UNIVERSIDADE DE SÃO PAULO
INSTITUTO DE FÍSICA DE SÃO CARLOS

GUSTAVO ANDRADE SILVA ALVES

Bi-doped NaTaO3 photocatalysts for hydrogen production under simulated sunlight: band gap narrowing and structural transitions

São Carlos
2021

GUSTAVO ANDRADE SILVA ALVES

Bi-doped NaTaO3 photocatalysts for hydrogen production under simulated sunlight: band gap narrowing and structural transitions

Dissertation presented to the Graduate Program in Physics at the Instituto de Física de São Carlos, Universidade de São Paulo to obtain the degree of Master of Science.

Concentration area: Applied Physics

Advisor:
Prof. Dr. Renato Vitalino Gonçalves

Corrected version
(original version available on the Program Unit)

São Carlos
2021

I AUTHORIZE THE REPRODUCTION AND DISSEMINATION OF TOTAL OR PARTIAL COPIES OF THIS DOCUMENT, BY CONVENTIONAL OR ELECTRONIC MEDIA FOR STUDY OR RESEARCH PURPOSE, SINCE IT IS REFERENCED.

Alves, Gustavo Andrade Silva
Bi-doped NaTaO3 photocatalysts for hydrogen production under simulated sunlight: band gap narrowing and structural transitions / Gustavo Andrade Silva Alves; advisor Renato Vitalino Gonçalves - corrected version -- São Carlos 2021.
71 p.

Dissertation (Master's degree - Graduate Program in Applied Physics) -- Instituto de Física de São Carlos, Universidade de São Paulo - Brasil , 2021.

1. Photocatalytic water splitting. 2. Doping. 3. Phase transition. I. Gonçalves, Renato Vitalino, advisor. II. Title.

ACKNOWLEDGEMENTS

I would like to acknowledge FAPESP for funding this research work through the project 2018/25705-0, as part of the program 2017/18716-3. This research used facilities of the Brazilian Nanotechnology National Laboratory (LNNano), part of the Brazilian Centre for Research in Energy and Materials (CNPEM), a private non-profit organization under the supervision of the Brazilian Ministry for Science, Technology, and Innovations (MCTI). The Transmission Electron Microscopy staff is acknowledged for the assistance during the experiment TEM-C1-27122-F.

This work has only been made possible due to the constant support of my advisor, professor Renato V. Gonçalves, who has always shared my enthusiasm with the project and has always been willing to openly discuss the directions of our research. Also fundamental was the collaboration of the NaCA group members, especially the colleagues from LAPNano: Higor A. Centurion, Andressa S. Correa, Washington Santa Rosa, Lucas G. Rabelo, Thalles T. A. Lucas e Maurício A. Melo Jr.

Finally, I am very thankful to my family and Michele dos Santos for deeply inspiring me to pursue my goals, despite all the difficulties.

ABSTRACT

ALVES, G.A.S. **Bi-doped NaTaO3 photocatalysts for hydrogen production under simulated sunlight**: band gap narrowing and structural transitions. 2021. 71 p. Dissertation (Master in Science) - Instituto de Física de São Carlos, Universidade de São Paulo, São Carlos, 2021.

In the global scenario of increasing environmental concerns over the dependence on fossil fuels, photocatalytic water splitting has been regarded as a promising method for the clean production of hydrogen fuel (H_2) from water and sunlight. Despite recent advancements, only a few materials can be efficiently applied as photocatalysts for this reaction. In this context, sodium tantalate ($NaTaO_3$) is highly active for H_2 evolution, although the wide band gap of 4.0 eV precludes its practical application for solar water splitting. Therefore, a variety of band-gap narrowing approaches for this compound have been recently proposed, including bismuth doping. In this work, Bi-doped $NaTaO_3$ with a nanocubic morphology has been obtained through a simple molten salt method, in order that Bi^{3+}-Ta^{5+} atomic substitutions promote the formation of midgap electronic states which allow the absorption of light from the simulated sunlight spectrum (AM 1.5G). X-ray diffraction results reveal that the orthorhombic perovskite structure of $NaTaO_3$ undergoes a structural transition to pseudocubic upon low-concentration (0.5-4 mol%) Bi-doping. Accordingly, the Bi-doped photocatalysts present considerable H_2 evolution under simulated sunlight, whereas pristine $NaTaO_3$ exhibits negligible activity in these conditions. The highest H_2 evolution rates are obtained with 3 mol% Bi-doped $NaTaO_3$, as a possible consequence of the conjunction between the narrowed band gap of 3.6 eV with the rectified Ta-O-Ta bond angles in the pseudocubic lattice. Moreover, the photocatalytic activity is further improved and kept stable for 110h of reaction after Ni co-catalysts are loaded onto Bi-doped $NaTaO_3$ by magnetron sputtering deposition, in order that the nanosized Ni particles may provide abundant surface reaction sites for the evolution of H_2.

Keywords: Photocatalytic water splitting. Doping. Phase transition.

RESUMO

ALVES, G.A.S. **Fotocatalisadores de NaTaO3 dopado com Bi para a produção de hidrogênio sob luz solar simulada**: diminuição da banda proibida e transições estruturais. 2021. 71 p. Dissertação (Mestrado em Ciências) - Instituto de Física de São Carlos, Universidade de São Paulo, São Carlos, 2021.

Em vista do cenário global de crescentes preocupações ambientais a respeito da atual dependência em combustíveis fósseis, a divisão fotocatalítica da água tem sido considerada uma das mais promissoras estratégias para a produção limpa de hidrogênio (H_2) a partir da água e da luz solar. Apesar dos avanços recentes, observa-se que poucos materiais podem ser aplicados de forma eficiente como fotocatalisadores para esta reação. Neste contexto, o tantalato de sódio ($NaTaO_3$) mostra-se altamente ativo para a evolução de H_2, ainda que sua larga banda proibida de 4.0 eV impeça sua aplicação prática sob luz solar. Portanto, diversos métodos para o estreitamento desta banda proibida tem sido recentemente propostos, sendo um destes a dopagem com bismuto. Neste trabalho, $NaTaO_3$ dopado com Bi foi produzido de forma simples pelo método de sal fundido, de modo que a substituição atômica Bi^{3+}-Ta^{5+} promove a formação de estados eletrônicos na região da banda proibida, permitindo assim a absorção de luz solar simulada (espectro AM 1.5G). Resultados de difração de raios-X revelam que a estrutura da perovskita ortorrômbica, característica do $NaTaO_3$ puro, se converte para uma perovskita pseudocúbica sob baixas concentrações do dopante (0.5-4 mol% Bi). Como consequência destas modificações, o fotocatalisador dopado com Bi apresenta uma significativa evolução de H_2 sob luz solar simulada, em contraste com a atividade nula do $NaTaO_3$ puro, sob estas mesmas condições. As mais altas taxas de produção de hidrogênio foram obtidas com $NaTaO_3$ dopado a 3 mol% Bi, possivelmente como resultado conjunto do band gap de 3.6 eV com os ângulos Ta-O-Ta retificados na rede pseudocúbica. Subsequentemente, a atividade catalítica é potencializada e se mantém estável por 110h após a deposição do cocatalisador Ni por pulverização catódica, evidenciando que as nanopartículas de Ni provém abundantes sítios ativos para a evolução de H_2 na superfície do $NaTaO_3$ dopado com Bi.

Palavras-chave: Divisão fotocatalítica da água. Dopagem. Transição de fase.

LIST OF FIGURES

Figure 1 Timeline of energy consumption and primary energy sources 19

Figure 2 World transportation consumption by fuel in 2012 (a), time series of atmospheric CO2 concentration obtained from ice cores (historical) and direct measurement (2005-present) (b) 20

Figure 3 Formation of bands due to overlapping atomic orbitals (a) and electronic band diagram of SrTiO3, showing the position of the Γ, X, M and R points in the cubic lattice (b) 22

Figure 4 Fundamental mechanism of overall water splitting, highlighting the steps of photon absorption (1), electron-hole recombination (2), separation (3) and surface redox reactions (4) 23

Figure 5 Standard solar spectrum AM 1.5G, highlighting the infrared, visible and ultraviolet regions (a), valence and conduction band positions of some typical materials for photocatalytic water splitting (b) 25

Figure 6 Structure of a cubic perovskite oxide (a), periodic table highlighting the elements that most commonly occupy A and B atomic sites in perovskite oxides (b)... 26

Figure 7 Distortions in the perovskite structure according to the Goldschmidt tolerance factor t (a) and comparison of the crystal field for Oh symmetry (cubic perovskite) and a distorted configuration (orthorhombic, rhombohedral or hexagonal perovskite) (b)... 27

Figure 8 Valence and conduction band positions of NaTaO3, in comparison with the redox potentials for water splitting (a), orthorhombic NaTaO3 structure (b) and electronic band structure calculated by DFT, with the respective density of states for orthorhombic NaTaO3 (c) 28

Figure 9 Pseudocubic lattice of NaTaO3, considered here as a monoclinic structure with β angles close to 90° (a), photoluminescence spectra, here employed as a technique for indicating radiative recombination, showing improved charge transport in pseudocubic NaTaO3 obtained by the sol-gel method (b) and photoluminescence spectra for NaTaO3 obtained by sol-gel (x = 0) and K-doped NaTaO3 (x = 0.01 to 0.2) obtained by the same method (c) 29

Figure 10 Proposed electron band diagrams for NaTaO3 and Bi-doped NaTaO3, considering substitution at Na, Ta or simultaneous Na and Ta atomic sites, as obtained by DFT calculation (a), photocatalytic hydrogen evolution under visible irradiation for Bi-doped NaTaO3, using CH3OH as a sacrificial reagent (b) 30

Figure 11 Crystallization mechanism of a molten salt method (a), NaTaO3 particles with a cubic morphology, obtained by the molten salt synthesis (b) 31

Figure 12 Examples of band diagrams and charge transfer processes for type-I (straddling), type-II (staggered) and type-III (broken gap) heterojunctions 32

Figure 13 Electronic band diagram for a p-n junction before contact between semiconductors (a) and after contact (b) 33

Figure 14 Possibilities of band alignment in junctions between a n-type semiconductor and metal with different fermi levels (a) and analogous band diagrams for p-type semiconductors (b) 34

Figure 15 Proposed mechanism for the formation of NaTaO3/Ni/NiO nanoparticles and the associated charge transport for overall water splitting (a), suggested band bending configuration for NaTaO3/Ni/NiO systems (b) ... 35

Figure 16 Basic mechanism of magnetron sputtering deposition with argon gas in a vacuum chamber (a) and nanoparticle formation as a result of a sputtering procedure over a powder support under stirring movement (b) 36

Figure 17 Main steps of the molten salt synthesis, showing the compounds that are present in each stage 37

Figure 18 Top view of the powder stirrer (a), formation of the argon plasma during sputtering deposition on the powder substrate (b) and the vacuum chamber that contains the sputtering setup (c) 38

Figure 19 Experimental setting for the photocatalytic water splitting reactions under simulated sunlight (a), Irradiation spectrum of the two systems employed as light sources in the work: The Xe lamp (red) and the Xe lamp + AM 1.5G system (blue) (b) 40

Figure 20 X-Ray diffraction patterns of NaTaO3 obtained by the molten salt method under different temperatures, in comparison with reference data for orthorhombic NaTaO3.. 41

Figure 21 SEM images of NaTaO3 obtained under 820 ºC (a), 900 ºC (b) 1000 ºC (c) and 1050 ºC (d) 42

Figure 22 Surface area of NaTaO3 samples produced at different temperatures, measured by multimolecular adsorption (BET method) 43

Figure 23 Hydrogen evolution in H2O + 20 vol% CH3OH for 25mg of NaTaO3 produced at different temperatures, using a Xe 300W lamp with 300 mW/cm2 power density 44

Figure 24 UV-vis spectrum of NaTaO3 obtained at varied temperatures, (a) suggested mechanism for the higher photocatalytic activity of NaTaO3 produced at 820 °C (b) 45

Figure 25 Hydrogen evolution in H2O + 20 vol% CH3OH for 25mg of 5 mol% Bi-doped NaTaO3 using the AM 1.5G solar simulator filter, with a Xe 300W lamp at a power density of 300 mW/cm2 47

Figure 26 Quartz reactor with H2O, methanol and 25 mg of 5 mol% Bi-doped NaTaO3, before and after AM 1.5G irradiation (a) and selected region in the wide scan XPS spectrum of 5 mol% Bi-doped NaTaO3, showing the calculated surface atomic ratio between Bi and Ta (b).............................. 48

Figure 27 SEM images of pristine (a) and Bi-doped NaTaO3 with 0.5 (b), 3 (c) and 5 (d) mol% Bi 49

Figure 28 TEM image of 3 mol% Bi-doped NaTaO3, (a) showing a magnified view of the region in the yellow square (b) 49

Figure 29 X-ray diffraction patterns from pristine and Bi-doped NaTaO3, showing wide scan profiles (a), the effect of doping on lattice expansion (b) and the different sub-peak pattern in orthorhombic and pseudocubic perovskite lattices (c)... 51

Figure 30 Raman scattering spectra of pristine and Bi-doped NaTaO3, highlighting the band related to the A1g vibrational mode, at approximately 863 cm-1 52

Figure 31 High-resolution X-ray photoelectron spectra of 3 mol% Bi-doped NaTaO3 (a), pristine NaTaO3 (b) and surface composition of the material, determined by XPS (c).. 54

Figure 32 UV-vis absorption spectra (a) and Tauc plots derived from each spectrum, considering different values for the r coefficient depending on the nature of the optical transition in Bi-doped and pristine NaTaO3 (b) 55

Figure 33 Electron band structure and density of states calculated for pristine orthorhombic NaTaO3 (a, b) and pseudocubic Bi-Ta doped NaTaO3 with O vacancies. (c, d) The dashed line marks the valence band maximum level of the pure model, in order to highlight the position of the energy level introduced by doping.. 56

Figure 34 Photocatalytic hydrogen evolution in H2O + 20 vol% CH3OH for 25mg of Bi-doped NaTaO3 under Xe 300W + AM 1.5G irradiation, at a power of 300 mW/cm2 (a) and schematic band diagram with the proposed charge transfer mechanism for Bi-doped NaTaO3 under AM 1.5G irradiation (b) 58

Figure 35 Photocatalytic hydrogen evolution in H2O + 20 vol% CH3OH for 25mg of 3 mol% Bi-doped NaTaO3 produced by different methods, under Xe 300W + AM 1.5G irradiation, at a power of 300 mW/cm2....................... 59

Figure 36 XRD spectrum of 3 mol% Bi-doped NaTaO3 produced by the solid state method at 1000°C (a) and highlighted regions in the XRD pattern, comparing the material obtained by solid state (blue) and molten salt (orange) showing the pseudocubic phase for both samples (b) 59

Figure 37 XPS survey spectrum comparing the surface concentration of Ni and Ta (a) XPS high-resolution spectrum of Ni 2p in 3 mol% Bi-doped NaTaO3 deposited with Ni for 10 min (b) 60

Figure 38 HAADF image with EDS mapping, showing the elemental composition of 3 mol% Bi-doped NaTaO3 loaded with Ni nanoparticles 61

Figure 39 Photocatalytic hydrogen evolution in H2O + 20 vol% CH3OH for Ni-loaded Bi-doped NaTaO3 under Xe 300W + AM 1.5G irradiation, at a 300 mW/cm2 power for varied sputtering deposition times (a) and during 100h of reaction (b), with the proposed charge transport mechanism (c) 62

LIST OF ABREVIATIONS AND ACRONYMS

BET	Brunauer-Emmett-Teller
CB	Conduction band
DC	Direct current
DFT	Density functional theory
DOS	Density of states
EDS	Energy-dispersive X-ray spectroscopy
HAADF	High-angle annular dark-field
HRTEM	High-resolution transmission electron microscopy
JCPDS	Joint committee on powder diffraction standards
NHE	Normal hydrogen electrode
SEM	Scanning electron microscopy
TEM	Transmission electron microscopy
UV	Ultraviolet
VB	Valence band
XPS	X-ray Photoelectron Spectroscopy
XRD	X-ray Diffraction

CONTENTS

1 INTRODUCTION 19

1.1 Background 19

1.2 Photocatalytic water splitting and the electronic structure of photocatalysts 21

1.3 The basic mechanism of photocatalytic water splitting 23

1.4 Photocatalyst materials for water splitting 24

1.5 Perovskite Oxides 26

1.6 Sodium tantalate ($NaTaO_3$) 27

1.7 Molten salt synthesis 31

1.8 Heterojunctions and co-catalysts 31

1.9 Magnetron sputtering deposition 35

2 MATERIALS AND METHODS 37

2.1 Materials and Reagents 37

2.2 Molten salt synthesis of $NaTaO_3$ 37

2.3 Molten salt synthesis of Bi-doped $NaTaO_3$ 37

2.4 Cocatalyst deposition 38

2.5 Material characterization 39

2.6 Photocatalytic hydrogen evolution 39

3 RESULTS 41

3.1 Production of pure $NaTaO_3$ 41

3.2 The influence of Bi doping on $NaTaO_3$ 46

3.3 Sputtering deposition of Ni co-catalysts over Bi-doped $NaTaO_3$ 60

4 CONCLUSIONS 63

REFERENCES 65

1 INTRODUCTION

1.1 Background

The use of fuels has been a fundamental and recurring practice for the human species throughout its entire history. Even before the emergence of the *homo sapiens*, the earlier *homo erectus* would probably begin to burn plant matter for cooking, protection and warmth, almost 1 million years ago. [1] As humans expanded and prevailed around the world, a wide variety of biomass fuels would be employed by early societies not only for strict survival purposes, but also for ceremonies, [2] and metal smelting. [3] Fossil fuels, such as coal and petroleum were probably first discovered and utilized in ancient China [4] and in the Near East, [5] but would only come into global prominence as valuable commodities a few centuries ago.

Fossil fuels consist of a wide variety of organic compounds formed by natural decomposition of ancient fossilized material, as a slow and complex route for energy storage in the form of chemical bonds. Therefore, this natural process is able to increase the enthalpy of combustion of dry biomass from approximately 20 kJ/g (wood) [6] to around 45 kJ/g (petroleum oil), [7] thus allowing for inexpensive practical application. During the Industrial Revolutions between the 18th and 19th centuries, the emerging production and consumption standards demanded for unprecedented amounts of fuels with a high energy density, thus making fossil fuels the ideal power sources for industry and transportation. [8] Since then, fossil fuels have been widely employed for powering vehicles, industrial processes and the generation of electricity, in a scenario of continuously rising energy consumption. Currently, as shown in Figure 1, 85% of the world's primary energy sources consist of fossil resources such as petroleum (34%), coal (27%) and natural gas (24%). [9]

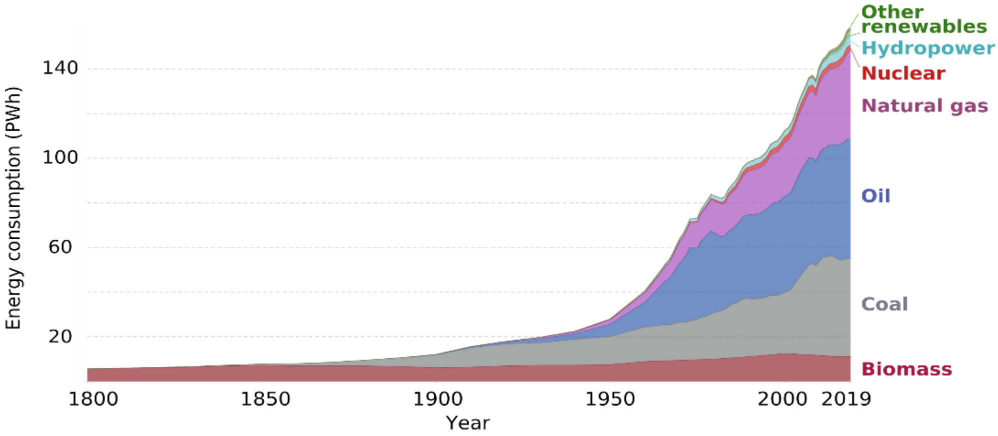

Figure 1 - Timeline of energy consumption and primary energy sources
Source: SMIL. [9]

Despite their short-term cost effectiveness, the widespread use of fossil fuels raises severe environmental and social worries. The large amounts of carbon dioxide (CO_2) released in combustion is the leading factor behind anthropogenic climate change, having been directly associated with temperature increase and ocean acidification in a global scale, thus threatening the sustenance of life on Earth. [10] As Figure 2b demonstrates, the concentration of atmospheric carbon dioxide has been rising sharply towards unprecedented levels, even when natural oscillations are taken into account. In addition to CO_2, the combustion of fossil fuels produces other compounds with detrimental environmental effects, such as CO, SO_x and NO_x. [11] Due to these issues, the current dependence on fossil fuels also entails hidden economic damage to society in the form of extreme weather events, food insecurity and health care costs, thus accounting for higher values than the after-tax profits for most fossil fuel companies. [12] Furthermore, as the formation of these resources takes millions of years, the perspective of reserve depletion, oscillating prices and political conflict in producer regions have been a constant matter of concern for the oil sector throughout the last decades. [13-14] Although the use of alternative fuels is becoming progressively significant in some sectors, about one quarter of all energy consumption in the world accounts for transportation, an area that is heavily dependent on petroleum derivatives, as shown in Figure 2a.

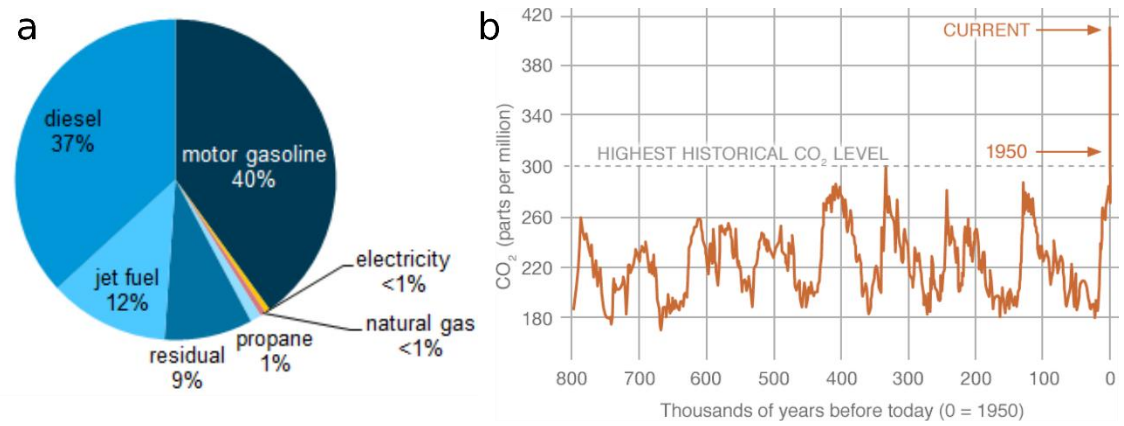

Figure 2 – World transportation consumption by fuel in 2012 (a), time series of atmospheric CO2 concentration obtained from ice cores (historical) and direct measurement (2005-present) (b).
Source: a) EIA; [15] b) NASA. [16]

In order to overcome the global dependence on carbon-based fuels, hydrogen gas (H_2) has been proposed as a clean an efficient alternative, since its combustion reaction only produces water vapour as a by-product. In virtue of its small molecular weight, hydrogen fuel has a higher energy density per mass in comparison to fossil resources, thus facilitating its application in vehicles. Accordingly, hydrogen fuel cell vehicles have been shown to offer a promising alternative for low-impact transportation, and their associated cost has been gradually reduced due to recent advancements. Other valuable applications of H_2 include the synthesis of ammonia (NH_3) and hydrochloric acid (HCl), as well as the reduction of ores into pure metals. [17]

Regardless of its status as a clean fuel, most of the world's hydrogen output is derived from steam reforming of methane (CH_4), which is in turn one of the main components of natural gas, mostly obtained from underground deposits. Together with oil reforming and coal gasification, these methods comprise 96% of the global hydrogen output. Therefore, commercial production of H_2 still relies heavily upon fossil fuels and releases CO_2 as part of the reform processes. Alternatively, a much smaller portion of hydrogen (4%) is produced from the electrolysis of H_2O, in which electric current is employed for water splitting without direct emission of pollutants. The necessity of an external power source may limit the efficiency and applicability of electrolysis, even though significant progress has been recently observed in this field. [18] In view of the present scenario, the development of new low-impact methods is thus necessary for a clean and economically viable production of hydrogen fuel at large scales.

1.2 Photocatalytic water splitting and the electronic structure of photocatalysts

Initially demonstrated by Honda and Fujishima in the 1970s, [19] Photocatalytic water splitting has been regarded as one of the most promising alternative methods for producing hydrogen with minimum environmental impact. Differently from electrolysis, it involves employing semiconductor materials as photocatalysts for obtaining H_2 from H_2O molecules, in a process entirely driven by sunlight. Therefore, in an analogous manner to photosynthesis, the technique is able to produce a fuel by directly utilizing the abundant energy from the sun. [20] With the growing understanding on the physics and chemistry of solids over the last decades, photocatalytic water splitting has been attracting considerable attention, as its efficacy relies heavily upon the electronic properties of these semiconductor materials. Furthermore, the development of nanoscale characterization and fabrication has brought several new possibilities for finely controlling morphology and surface properties of the photocatalysts. [21]

While electrons in isolated atoms occupy orbitals with discrete energy levels, solids exhibit a more complex set of features: as atoms are more closely packed, orbitals can overlap, thus giving rise to energy bands. This effect can be described as a consequence of the Pauli exclusion principle, since the presence of multiple atomic orbitals in the solid implies that energy levels have to split in order to prevent electrons from having the same quantum numbers.

Given the large density of overlapping atomic orbitals in a solid, these bands are practically continuous energy ranges, as these levels are very closely spaced from each other. Nonetheless, orbitals that are more spatially localized tend to overlap less with other orbitals, in order that some energy ranges may not be covered by any bands, as illustrated in Figure 3a. Accordingly, the range where no electronic states can exist is denominated as the band gap. [22-23]

A more detailed representation of the electronic band structure can be achieved by employing Density Functional Theory (DFT) as a computational tool for predicting the energy levels of many-electron systems. The method fundamentally consists of solving a set of Schrodinger-like equations, while considering the effect of an external potential, which is determined by the elemental composition and the system geometry. [24] Therefore, as illustrated in Figure 3b, the application of DFT-based models to crystalline solids is able to provide the electron energy levels for any direction in the crystal lattice, thereby presenting a 3-dimensional description of the electronic bands for a given material.

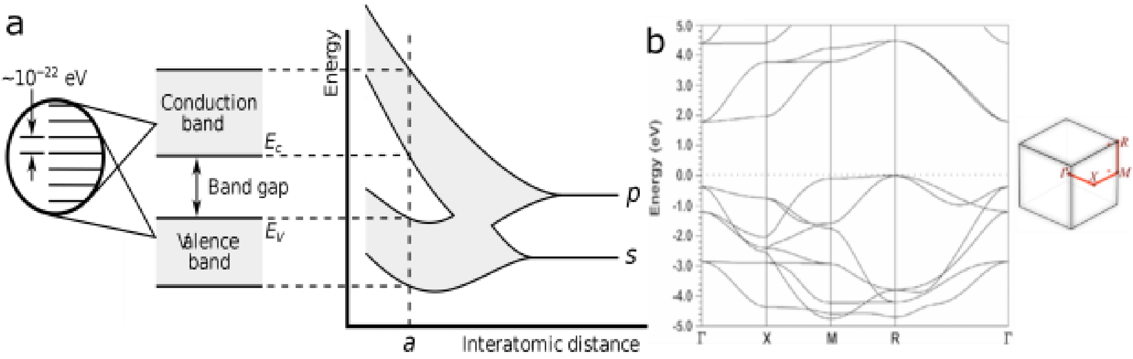

Figure 3 - Formation of bands due to overlapping atomic orbitals (a) and electronic band diagram of SrTiO3, showing the position of the Γ, X, M and R points in the cubic lattice (b)
Source: a) WIKIMEDIA; [25] b) ZHANG *et al.* [26]

In semiconductors and insulators at thermal equilibrium, a band gap separates states that are mostly occupied by electrons (valence band) from unoccupied states (conduction band). In virtue of this gap, electron transport is debilitated in these materials, in contrast with conductors, whose valence and conduction bands are strongly overlapped. Due to these properties, however, a wide variety of practical applications is made possible through the processes of charge generation and recombination, such as the emission and detection of light, as well as its use for photocatalytic reactions.

1.3 The basic mechanism of photocatalytic water splitting

The water splitting mechanism, illustrated in Figure 4, ideally involves four fundamental steps. In step 1, The first phenomenon consists in the absorption of photons by the semiconductor, which can excite electrons from the valence band to the conduction band. The collective effect of this process is analogous to the creation of an electron (negative potential) in the CB and a hole (positive potential) in the VB. [23]

Since excited electrons naturally tend to return to lower energy states, electron-hole recombination (step 2) takes place shortly after the excitation, thereby leading to energy release in the form of phonons (non-radiative) or photons (radiative recombination). [27] This effect imposes a significant constraint to photocatalysis, as it prevents most charge carriers from reaching the material surface, where surface reactions may take place.

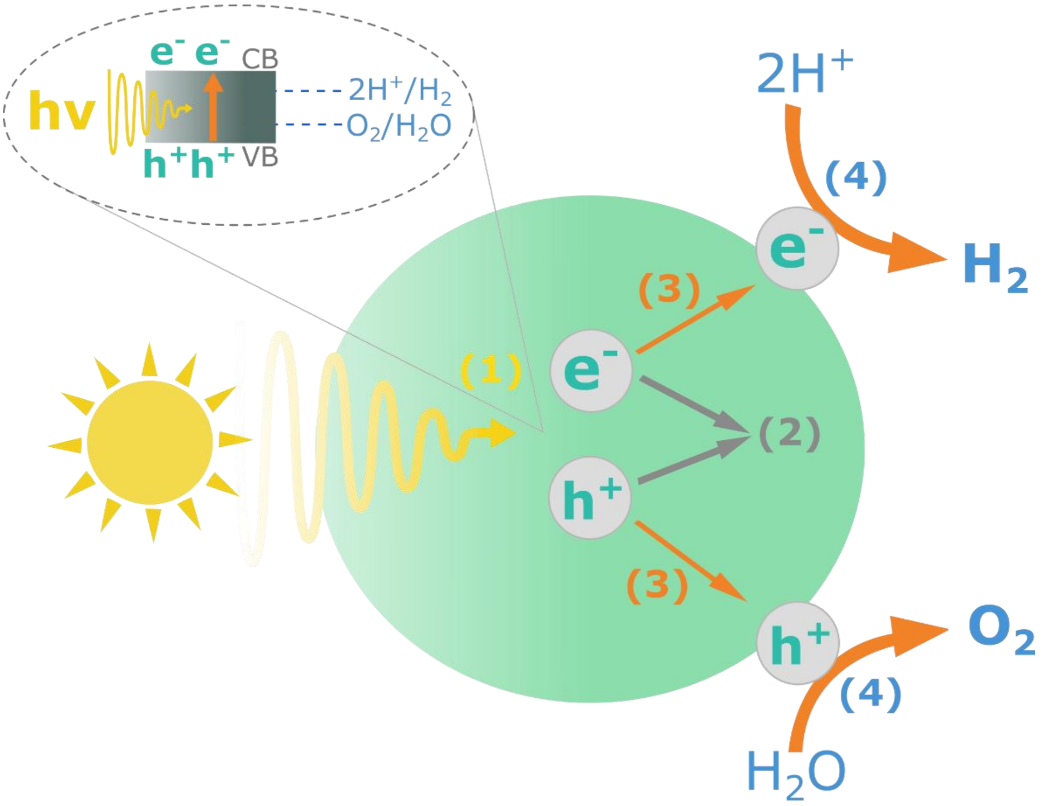

Figure 4 - Fundamental mechanism of overall water splitting, highlighting the steps of photon absorption (1), electron-hole recombination (2), separation (3) and surface redox reactions (4)
Source: By the author

In step 3, some electrons and holes must be effectively separated and driven to the semiconductor surface. This charge transfer process is mostly dependent on structural and electronic properties of the photocatalysts, in order that a high mobility of photogenerated charge carriers is essential for the photocatalytic activity.

Subsequently, in the presence of adsorbed H_2O at the semiconductor surface, electrons can provide a negative potential for the reduction of protons, while holes can oxidise water molecules, as part of step 4. Therefore, this chain of effects may ideally lead to the splitting of H_2O into hydrogen (H_2) and oxygen gas (O_2), if the photocatalyst material presents adequate properties in terms of electronic structure, charge transport, surface composition and morphology. [28] However, in practical application under natural sunlight, this reaction is often limited by rapid electron-hole recombination rates, in order that the water splitting reaction may only be observed in the presence of sacrificial reagents or by employing a high irradiation power. For this reason, the development of efficient photocatalysts for overall water splitting in a large scale still remains an unaccomplished goal.

1.4 Photocatalyst materials for water splitting

In virtue of the described mechanism, the photocatalytic process is only allowed to take place if electrons and holes have enough energy to overcome the redox potentials for each half reaction of water splitting. Accordingly, the CB potential must be more negative than the potential for the H^+/H_2 reduction (0 eV vs. NHE), while the VB level has to be more positive than 1.23 eV vs. NHE, which is the redox potential for the O_2/H_2O oxidation. For this reason, only semiconductors with a minimum band gap of 1.23 eV can split water molecules through this method. [28] Therefore, as shown in the solar spectrum in Figure 5a, only photons with energies within 1.23 eV (near-infrared) and approximately 3.70 eV (near-ultraviolet) can be utilized as the energy source for photocatalytic water splitting under natural sunlight. Considering these band gap criteria, Figure 5b shows examples of some semiconductors that have been proposed as photocatalysts for water splitting, given their adequate band structure for this application. In result of the sufficient potentials for proton reduction and water oxidation, materials such as $NaTaO_3$ are able to carry out overall water splitting, while other semiconductors can only conduct either hydrogen or oxygen evolution reactions, as observed for Cu_2O and WO_3, respectively. Furthermore, in order to conduct a single half-reaction, sacrificial reagents may be employed as electron- or hole-acceptors, in order that charge carriers which cannot react with H_2O are transferred to these compounds, thereby inhibiting recombination to some extent. [20]

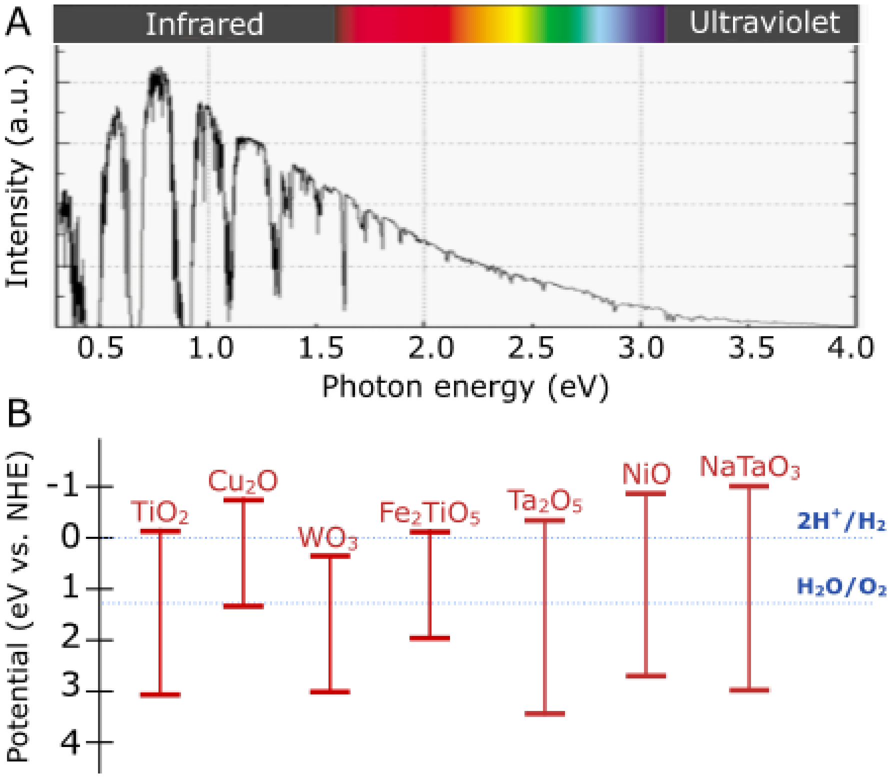

Figure 5 - Standard solar spectrum AM 1.5G, highlighting the infrared, visible and ultraviolet regions (a), valence and conduction band positions of some typical materials for photocatalytic water splitting (b).
Source: a) Adapted from NREL; [29] b) Adapted from LU *et al.*; [30] KALANUR *et al.*; [31] and MELO *et al.* [32]

In addition to limitations regarding the band gap, electron-hole recombination poses a significant constraint to water splitting. Whereas H_2 and O_2 evolution reactions occur within microseconds or milliseconds, recombination happens in the picosecond range. Therefore, the faster nature of this process prevents charge carriers from reaching the photocatalyst surface, thereby inhibiting reactions with H_2O molecules. Although bulk recombination is inherent to the photon absorption process, discontinuities in the semiconductor lattice, such as atomic vacancies, impurities, surfaces and interfaces may lead to trap states that aggravate carrier recombination. For efficient solar water splitting, it is therefore essential that photoinduced electrons and holes are effectively separated and directed towards surface reaction sites. [33]

Considering practical applications, ideal materials for photocatalytic water splitting should present adequate valence and conduction band potentials that allow absorption of natural sunlight. Moreover, the semiconductor must simultaneously have high charge carrier mobility and stability in aqueous media. So far, no semiconductor has been able to meet all these criteria for hydrogen production at large scales, and only few materials can be regarded as promising candidates.

1.5 Perovskite Oxides

Among the suitable materials for water splitting, perovskite oxides such as $SrTiO_3$, $KTaO_3$ and $NaTaO_3$ can be highlighted in virtue of their high stability and the broad possibilities for structural modification, which allows some of their electronic properties to be finely tuned by doping with a wide range of elements. [34] These crystal structures feature the ABO_3 formula, and are typically represented as in Figure 6a, with a central cation A surrounded by eight BO_6 octahedrons. This specific atomic arrangement implies geometric restrictions to lattice atoms, since the A-site is able to accommodate larger cations than the B-site. [35] Correspondingly, Figure 6b shows the atomic position that each chemical element is more likely to occupy in the perovskite structure.

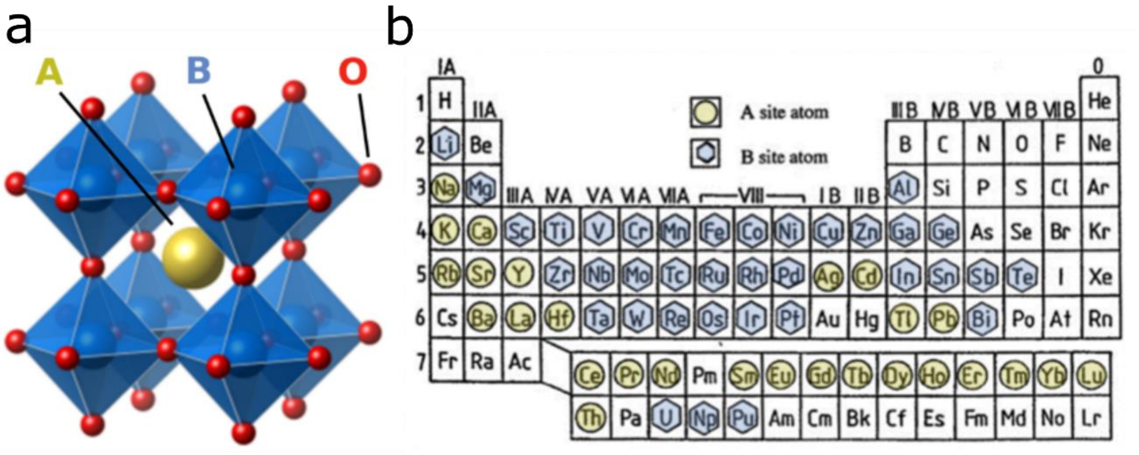

Figure 6 – Structure of a cubic perovskite oxide (a), periodic table highlighting the elements that most commonly occupy A and B atomic sites in perovskite oxides (b)

Source: a) By the author; b) Adapted from ISHIHARA. [35]

In virtue of these geometric criteria, the stability of ABX_3 perovskites can be reasonably predicted through a simple approach, which consists in determining the Goldschmidt Tolerance Factor for a given combination of A, B and X chemical elements. Assuming each constituent ion as a hard sphere with a Shannon ionic radius R, the factor t estimates whether the A cation is able to fit in the cavities between BO_6 octahedrons. Therefore, considering these geometrical arguments, the Goldschmidt Tolerance Factor is defined by the following formula: [36]

$$t = \frac{R_A + R_X}{\sqrt{2}(R_B + R_X)}$$

Accordingly, as illustrated in Figure 7a., ideal perovskites with a cubic structure feature Goldschmidt factors between 0.9 and 1, whereas values that deviate from this range indicate substantially distorted structures. For $t > 1$, A-site cations are too large, and the perovskite structure is not formed, while *t* values slightly below 0.9 represent smaller A cations, which promote distorted BO_6 octahedrons, as a characteristic feature of orthorhombic perovskites. Correspondingly, the increasing degree of distortion near $t = 0.8$ prevents the formation of the perovskite structure, thus making rhombohedral structures more energetically favourable under these conditions. [37]

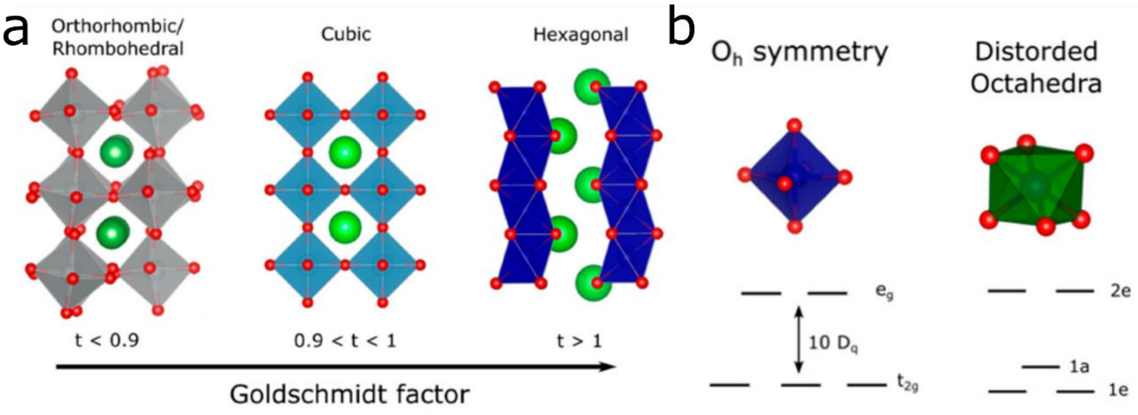

Figure 7 - Distortions in the perovskite structure according to the Goldschmidt tolerance factor t (a) and comparison of the crystal field for Oh symmetry (cubic perovskite) and a distorted configuration (orthorhombic, rhombohedral or hexagonal perovskite) (b).

Source: YANG *et al.* [37]

As illustrated in Figure 7b, the distortion of BO_6 octahedrons in the perovskite lattice may lead to noticeable modifications in the electronic levels of the material, due to the lowered symmetry. Consequently, inhibiting or inducing octahedral tilting in perovskite oxides may offer the possibility of tuning a wide range of properties in these materials. [38-39]

1.6 Sodium tantalate ($NaTaO_3$)

As one of the materials with the most expressive photocatalytic activity for hydrogen production under UV light, $NaTaO_3$ has attracted considerable interest over the past few decades. This remarkable activity can be mostly ascribed to the highly negative potential of its conduction band, as shown in Figure 8a, which provides considerable energy for the reduction of protons in H_2O. Likewise, the favourable position of its valence band also allows $NaTaO_3$ to be active for overall water splitting, even in its pure form. However, due to its wide band gap of 4.0 eV, this high activity is limited to ultraviolet light, and photons from the solar spectrum are not sufficiently energetic to excite $NaTaO_3$. [40-41]

Considering the ionic radii for Na^+ (102 nm), Ta^{5+} (64 nm) and O^{2-} (140 nm), $NaTaO_3$ presents a tolerance factor of 0.84, which indicates a significant degree of distortion with respect to an ideal perovskite. Accordingly, the vast majority of synthesis methods, including solid-state [40], molten salt,[42] hydrothermal,[43] solvothermal [44] and chemical vapor deposition [45] produce $NaTaO_3$ in the form of a *Pnmb* orthorhombic perovskite, as illustrated in Figure 8b. In Figure 8c, the density of states (DOS) derived from the electronic band structure of $NaTaO_3$ reveals that its valence and conduction bands are mostly composed of Ta 5d and O 2p orbitals, which are far more delocalized than Na 2s electrons. Therefore, most of the relevant processes for charge transport in $NaTaO_3$ are usually described in terms of Ta-O bonds or TaO_6 octahedrons.

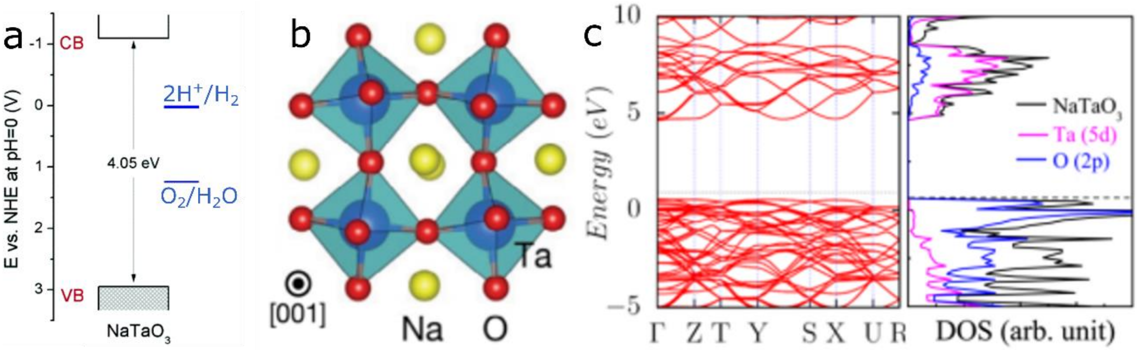

Figure 8 - Valence and conduction band positions of NaTaO3, in comparison with the redox potentials for water splitting (a), orthorhombic $NaTaO_3$ structure (b) and electronic band structure calculated by DFT, with the respective density of states for orthorhombic $NaTaO_3$ (c)
Source: a) Adapted from FRESNO *et al.;* [46] b) ONISHI; [47] c) MODAK *et al.* [48]

Although orthorhombic $NaTaO_3$ is highly more prevalent at room temperature, neutron diffraction studies at high temperatures show that a phase transition above 450 ºC leads to a Cmcm orthorhombic structure with similar a, b and c lattice parameters, which can be considered a pseudocubic perovskite with nearly undistorted TaO_6 octahedrons, similarly as seen in Figure 9a. Recently, it has been shown that this pseudocubic structure may also arise as a common secondary phase in orthorhombic $NaTaO_3$ at room temperature, [49] and it may become more prominent with the introduction of compositional impurities, such as K, Ca and Ti dopants. [50]

Pseudocubic $NaTaO_3$ with advantageous properties for water splitting has been first reported as a result of the sol-gel synthesis. [51] This phase has been suggested to be superior with respect to the most common form, as it presents an indirect band gap [52] and Ta-O-Ta bond angles closer to 180º, which provide greater energy delocalization for conduction band levels. [41] Therefore, these intrinsic features of pseudocubic $NaTaO_3$ may be associated with improved charge carrier separation, as evidenced by the lower photoluminescence intensities for the material obtained by sol-gel, in Figure 9b. Coherently, the addition of potassium as a dopant in the sol-gel synthesis provided further rectification of the structure, thus leading to lowered charge recombination,[53] as shown in Figure 9c. Nevertheless, the exact mechanism that explains the unexpected formation of pseudocubic $NaTaO_3$ at room temperature remains unknown, and only a few techniques for obtaining this phase have been reported so far.

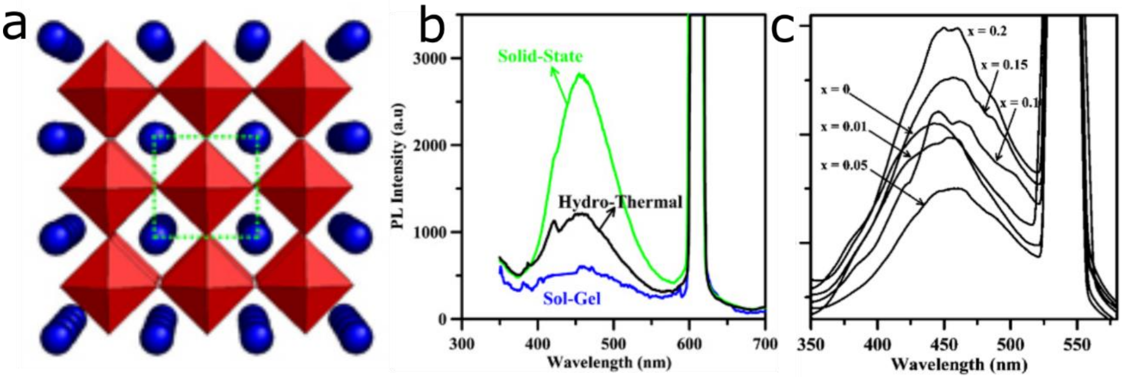

Figure 9 – Pseudocubic lattice of $NaTaO_3$, considered here as a monoclinic structure with β angles close to 90° (a), photoluminescence spectra, here employed as a technique for indicating radiative recombination, showing improved charge transport in pseudocubic $NaTaO_3$ obtained by the sol-gel method (b) and photoluminescence spectra for $NaTaO_3$ obtained by sol-gel ($x = 0$) and K-doped $NaTaO_3$ ($x = 0.01$ to 0.2) obtained by the same method (c)

Source: a) and b) HU *et al.;* [54] c) HU *et al.* [53]

Due to its wide band gap, $NaTaO_3$ can only absorb ultraviolet irradiation, thereby hindering its practical application under natural sunlight. Accordingly, doping and heterojunction approaches have been considered, as potential ways to overcome this drawback by altering the electronic band structure and improving charge transfer properties in the material.[34]

Some doping approaches have achieved significant progress in enhancing the photocatalytic activity of $NaTaO_3$. Some of the most successful strategies consist of La^{3+} [55] and Sr^{2+} [47] doping, which are shown to enhance charge transfer [56-57] and promote surface reconstruction with the formation of step-like nano-structures that multiply the available area for water splitting reactions.[58] Regardless of these favourable effects, Sr and La doping are only beneficial to hydrogen evolution under UV light, since these dopants show no influence on the band gap. Alternatively, a few co-doping methods, such as La/Fe and La/Cr can induce band gap narrowing by creating midgap electron states, therefore enabling H_2 evolution under visible light.[59-60]

Recently, bismuth has been shown to be an effective dopant for making $NaTaO_3$ active for hydrogen production under visible irradiation. Density functional theory studies have pointed out that Bi^{3+} cations are able to replace both Na^{+} and Ta^{5+} in the perovskite lattice, depending on the stoichiometry of the precursors. Accordingly, a Na-rich reaction environment favors doping at the Ta^{5+} site, while Na-poor conditions are more likely to promote the substitution of Na^{+}. Subsequently, electronic band structures calculated by DFT, in Figure 10a, reveal that doping on these different atomic sites can lead to distinct electron band structure configurations, and band gap narrowing is only possible in virtue of Bi^{3+}-Ta^{5+} substitution. [61] Accordingly, as illustrated in Figure 10b, experimental works have demonstrated hydrogen evolution under visible light with Bi-doped $NaTaO_3$ obtained by hydrothermal, [62] spray pyrolysis [63] and solid state methods. [64] In these examples, Bi has been reported to promote only slight distortions in the orthorhombic $NaTaO_3$ lattice, and the highest H_2 production rates are reported at Bi concentrations between 7 and 8 mol%.

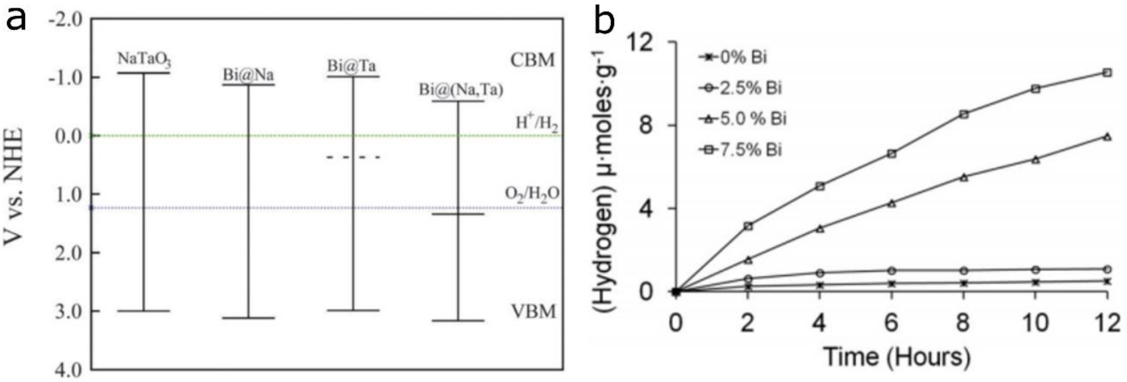

Figure 10 - Proposed electron band diagrams for $NaTaO_3$ and Bi-doped $NaTaO_3$, considering substitution at Na, Ta or simultaneous Na and Ta atomic sites, as obtained by DFT calculation (a), photocatalytic hydrogen evolution under visible irradiation for Bi-doped $NaTaO_3$, using CH_3OH as a sacrificial reagent (b)

Source: a) JOO *et al.;* [61] b) KANHERE *et al.* [64]

Even though the reported doping methods are efficient for the band gap narrowing of $NaTaO_3$, hydrogen evolution under visible irradiation is considerably low with respect to the rates obtained using ultraviolet light. This suggests that the doped material may present limited charge transport properties. Furthermore, the influence of low Bi doping concentrations (<5 mol%) has remained mostly unexplored.

One of the most common doping approaches for perovskite oxides consists in the introduction of a dopant precursor with the usual reactants of the solid state synthesis. This facile method often may provide a significant amount of energy for the formation of the doped phase, given the high temperatures of the synthesis procedure. However, the material produced by the solid state approach may not always present an adequate morphology for photocatalytic applications, as particles often lack exposed facets for surface reactions and their surface area may be lower with respect to other synthesis methods. [65]

1.7 Molten salt synthesis

The molten salt method consists of a modified form of the solid state reaction, having been widely utilized for producing single crystals and ceramic powders. Typically, it consists of employing a molten salt as the reaction medium for obtaining complex oxides from carbonates and oxide precursors. As illustrated in Figure 11a, the method allows reactants to dissolve and diffuse homogeneously when temperatures above the salt melting point are reached. During the calcination procedure, this liquid environment provides increased reaction rates and improved homogeneity. Subsequently, nucleation of the final product occurs at the surface of reactant particles, prior to precipitation upon cooling. A remarkable feature of this synthesis method is that the dimension and shape of particles can be often finely controlled by tuning calcination temperatures, salt composition and reactant/salt quantities. [66]

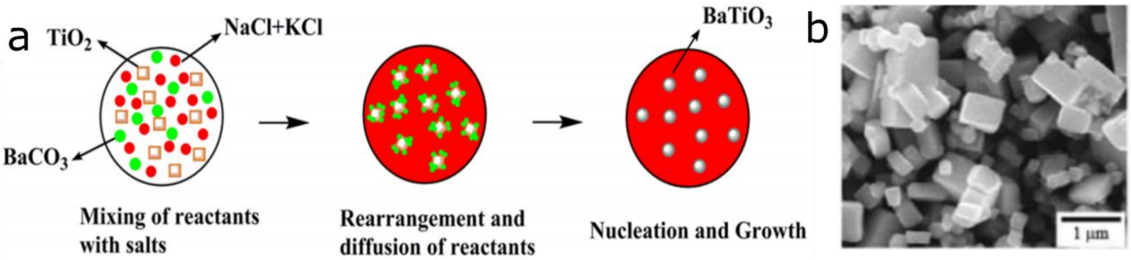
a
TiO_2
NaCl+KCl
$BaCO_3$
Mixing of reactants with salts
Rearrangement and diffusion of reactants
$BaTiO_3$
Nucleation and Growth
b
1 μm

Figure 11 – Crystallization mechanism of a molten salt method (a), NaTaO3 particles with a cubic morphology, obtained by the molten salt synthesis (b)
Source: a) FU *et al.;* [67] b) LEE *et al.* [68]

Although this method has been employed for obtaining bulk materials over the past decades, recent progress in developing nanostructured oxides has brought renewed interest towards the molten salt synthesis. As an example, Figure 11b shows cubic $NaTaO_3$ particles with dimensions between 200 nm and 1 µm, whose morphology can be controlled by using different calcination temperatures and salt quantities. [68]

1.8 Heterojunctions and co-catalysts

The combination of semiconductors with different band gaps is often beneficial for photocatalytic water splitting. Depending on how electronic band levels are aligned with respect to the potentials for oxidizing H_2O and reducing H^+, charge transfer mechanisms can be controlled in heterostructured materials. Accordingly, Figure 12 illustrates the 3 typical types of semiconductor heterojunctions in terms of band alignment, considering that coulombic interactions drive electrons towards more positive potentials, while holes proceed oppositely.

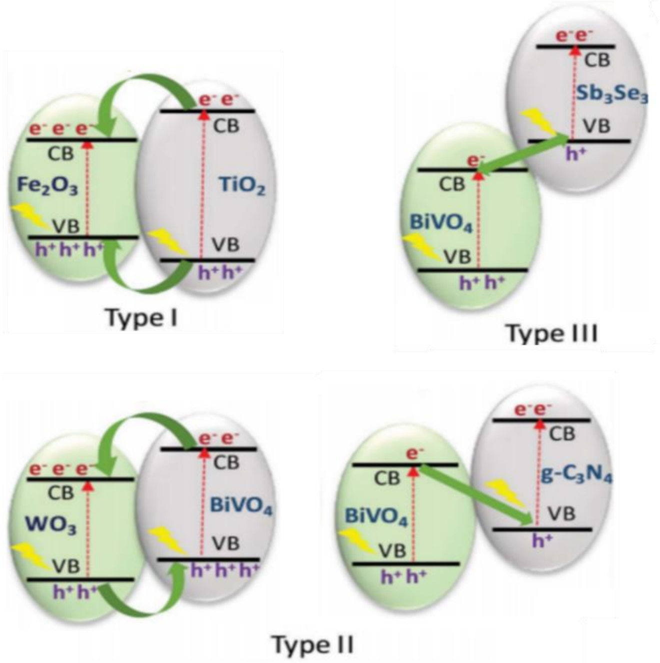

Figure 12 – Examples of band diagrams and charge transfer processes for type-I (straddling), type-II (staggered) and type-III (broken gap) heterojunctions

Source: Adapted from AFROZ *et al.* [69]

Upon light excitation of a Type-I junction, both photogenerated electrons and holes tend to be transported to the semiconductor with the smaller gap, as illustrated in Figure 12 for the TiO_2/Fe_2O_3 system. As this heterostructure concentrates electrons and holes in the same semiconductor with the smaller band gap, recombination may remain a significant limiting factor in this example. In the Type-II arrangement, however, the band levels favour the spatial separation of charge carriers, as electrons and holes are directed towards distinct materials. Simultaneously, electrons from the conduction band of one semiconductor may also undergo recombination with the holes from the other material, as exemplified in Figure 12. Differently from these examples, Type-III heterojunctions feature no overlap between bands, thus lessening charge transfer between semiconductors. In view of these distinct possibilities, Type-II heterojunctions usually offer the most adequate conditions for photocatalytic water splitting, given the importance of charge carrier separation in this application. [69]

Determining precise band diagrams for a heterojunction can be a challenging task, since the band energy levels of a material may be different with respect to the pure semiconductor. When two materials with distinct Fermi levels come into contact, as in Figure 13a, an electric field arises at the interface, as a result of the energy offset between the Fermi levels. Subsequently, valence and conduction bands undergo a shift as an equilibrium state is reached, with the two semiconductors having the same Fermi level. The inherent band discontinuity at the junction interface implies that there must be some degree of band bending in order to keep the vacuum level continuous and the Fermi level constant in the entire material, as shown in Figure 13b. [70] In view of these effects, some heterojunctions may feature significant band diagram shifts in comparison with the pure materials, as the example for a p-n junction in Figure 13 illustrates. Since band bending arises due to the Fermi level offset, semiconductor junctions in which these levels are similar may not present this pronounced effect.

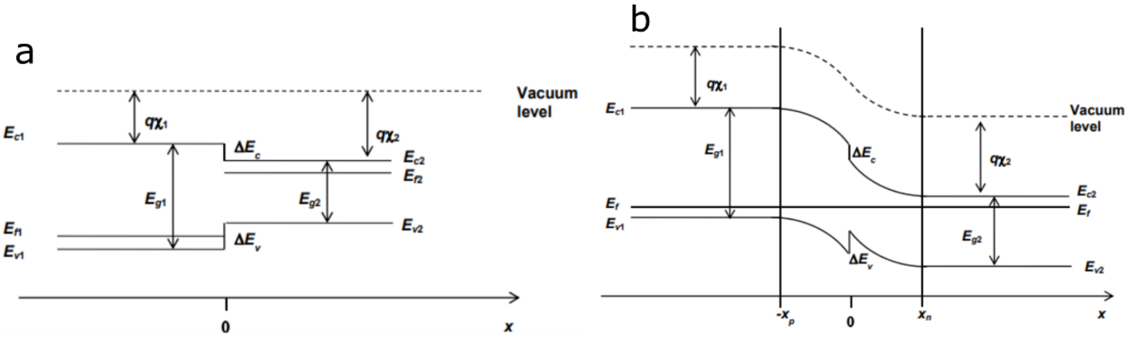

Figure 13 – Electronic band diagram for a p-n junction before contact between semiconductors (a) and after contact (b)

Source: Adapted from RANA. [70]

Another type of heterostructure that finds high relevance in photocatalytic water splitting is the semiconductor-metal junction. As shown in Figure 14a, band bending may occur differently depending on the energy difference between metal and semiconductor Fermi levels. If the n-type semiconductor has a higher (more negative) Fermi level, electrons flow towards the metal upon contact, and when equilibrium is reached, the interface develops a depletion layer due to the lower concentration of free electrons in the semiconductor. In this case, band bending promotes the formation of a Schottky barrier, which favours charge transfer from semiconductor to the metal. On the other hand, if the metal has the highest Fermi level, electron transport occurs in the opposite direction when contact occurs, and an accumulation layer arises in the interface region, which subsequently allows transport of charge carriers in both directions. Due to this resistive character, this last type of contact is designated as an ohmic junction.[71] Figure 14b illustrates that a similar mechanism is established for p-type semiconductors, in which holes are the majority carrier for charge transfer. Since in this case hole transport must be considered, a Schottky contact is established if the metal has a more negative Fermi level than the semiconductor, thereby promoting hole transfer towards the metal. Analogously, if the semiconductor has the highest Fermi level, an ohmic junction is formed.

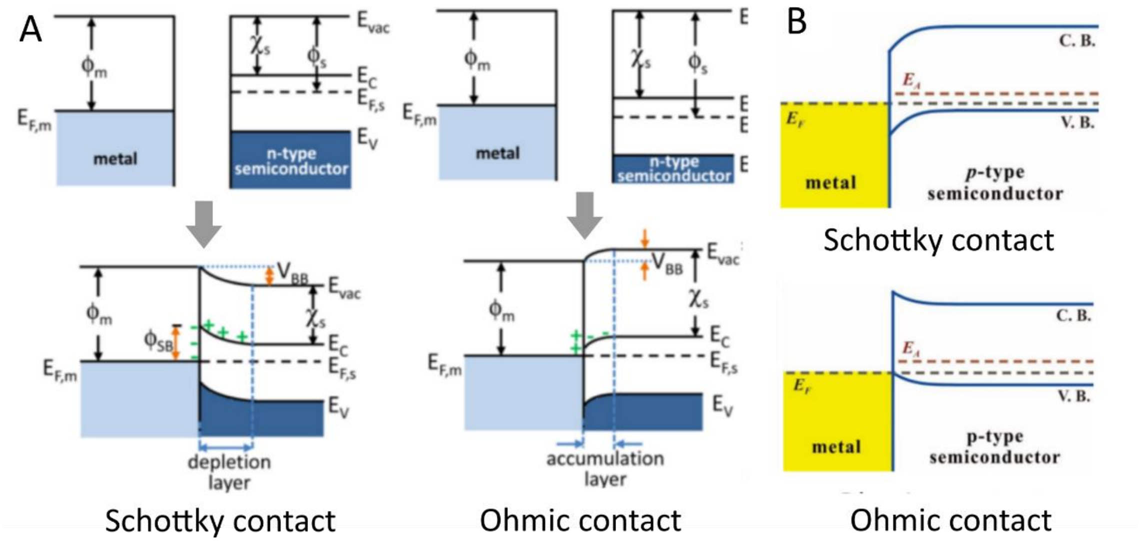

Figure 14 – Possibilities of band alignment in junctions between a n-type semiconductor and metal with different fermi levels (a) and analogous band diagrams for p-type semiconductors (b)
Source: a) Adapted from ZHANG *et al.;* [71] b) Adapted from POLETI *et al.* [72]

Given the rapid recombination of photogenerated charge carriers during photocatalytic reactions, co-catalysts consisting of metallic particles have been widely employed for enhancing electron-hole separation. A key aspect of these systems involve the formation of a Schottky barrier at the semiconductor-metal interface, which may trap photogenerated electrons in the co-catalyst, where hydrogen evolution reactions can take place. Therefore, adequate co-catalysts deposited at the photocatalyst surface are able to provide redox reaction sites, thereby significantly inhibiting bulk recombination. As the formation of this barrier relies upon the difference between metal and semiconductor Fermi levels, some metal-semiconductor combinations may be more effective than others for optimized charge carrier separation. [73-74] Nevertheless, a variety of other factors may influence charge transport in semiconductor-metal systems, such as lattice matching and the adhesion between these materials. [75]

As a relevant example of an advantageous metal-semiconductor contact for solar water splitting, Ni and NiO have been the most widely employed co-catalysts for $NaTaO_3$, although the exact charge transport mechanism for these junctions still remains a matter of debate. As illustrated in Figure 15a, both Ni an NiO may often be present in the aqueous medium, since an oxide layer is typically formed over Ni particles, and NiO can be also photoreduced to Ni. Therefore, photogenerated electrons from $NaTaO_3$ may migrate to Ni particles where H_2 evolution occurs, whereas holes are directed towards O_2 evolution sites in NiO. [76] Moreover, it has been suggested that band bending might play an important role in $NaTaO_3$/Ni/NiO systems. Considering the double junction as in Figure 15b, the presence of a Schottky contact between $NaTaO_3$ and Ni may allow the injection of photogenerated electrons from $NaTaO_3$ into the

Ni/NiO system, where the ohmic junction between Ni and NiO promotes free charge transport across this interface. Subsequently, hydrogen evolution could be possible in either Ni or NiO sites. [77]

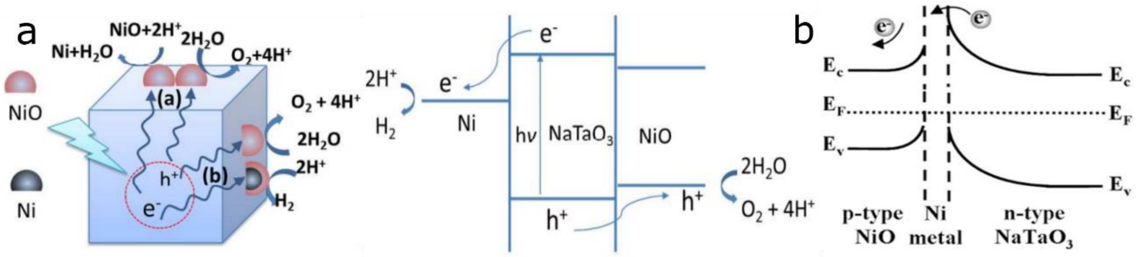

Figure 15 – Proposed mechanism for the formation of NaTaO3/Ni/NiO nanoparticles and the associated charge transport for overall water splitting (a), suggested band bending configuration for NaTaO3/Ni/NiO systems (b).

Source: a) ZHANG *et al.;* [76] b) HU *et al.* [77]

During overall water splitting reactions, charge separation can be further improved by depositing distinct co-catalysts for hydrogen and oxygen evolution reactions. Therefore, while metal particles provide proton reduction sites for electrons, metals oxides such as CoO_x and RuO_x are typically utilized as co-catalysts for water oxidation. In addition to improving charge transport, oxygen evolution co-catalysts may also prevent the undesired self-oxidation of the main photocatalyst by photogenerated holes. [73]

In general, co-catalysts for water splitting can be loaded on photocatalyst substrates by a wide variety of methods, including photodeposition impregnation, [76] magnetron sputtering [78] and electrodeposition procedures. [79] These approaches may largely differ in terms of particle size, shape and crystallinity, as well as with respect to the adhesion between co-catalysts particles and the substrate material.

1.9 Magnetron sputtering deposition

The magnetron sputtering technique consists essentially in the deposition of ejected atoms from a solid target that is bombarded by energetic ions. As illustrated in Figure 16a, the application of voltage between the target and the substrate holder in a high vacuum environment promotes the formation of a plasma discharge, which is concentrated near the target by an arrangement of magnets. Accordingly, atoms from the ionized gas collide with the solid, in order that the removed atoms are deposited over a substrate situated in front of the target. [80]

Since this process does not involve the addition of external reactants, sputtering deposition has been widely used as a method to produce high-quality thin films and nanoparticles over planar,[80] liquid [81] and powder substrates. [82]

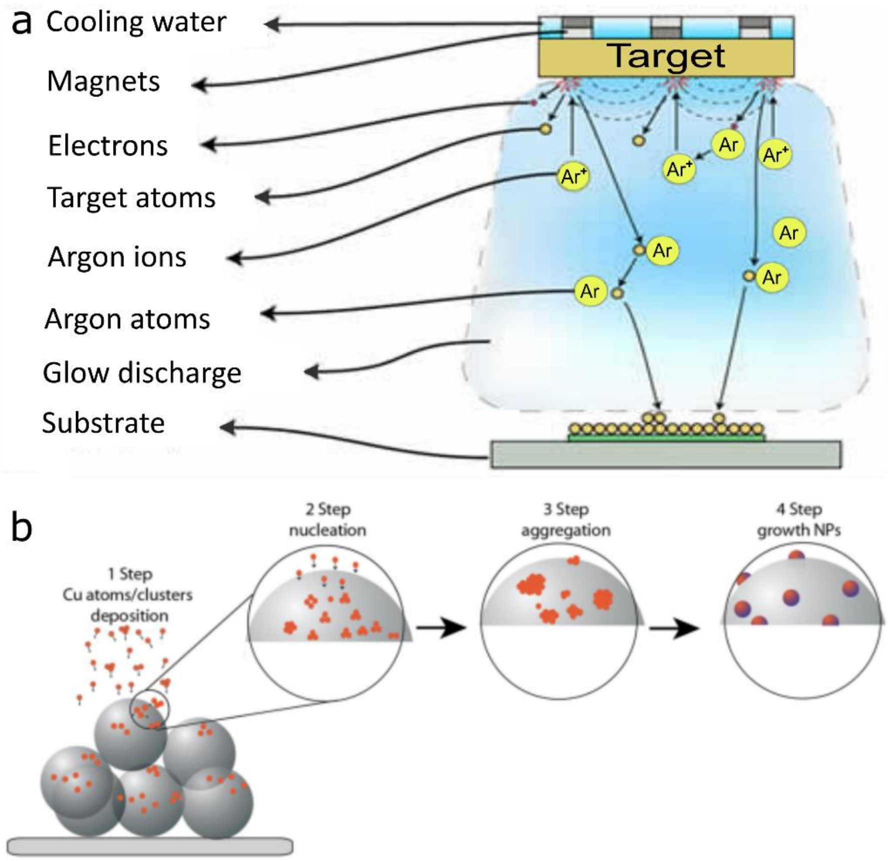
a
Cooling water
Magnets
Electrons
Target atoms
Argon ions
Argon atoms
Glow discharge
Substrate
Target
Ar
Ar+
b
1 Step
Cu atoms/clusters
deposition
2 Step
nucleation
3 Step
aggregation
4 Step
growth NPs

Figure 16 – Basic mechanism of magnetron sputtering deposition with argon gas in a vacuum chamber (a) and nanoparticle formation as a result of a sputtering procedure over a powder support under stirring movement (b).
Source: a) Adapted from XIAO; [83] b) Adapted from GONÇALVES *et al.* [82]

Due to these features, magnetron sputtering deposition on powder substrates can be regarded as a highly promising technique for obtaining particulate heterogeneous materials for water splitting, as it allows the deposition of well-dispersed nanoparticle co-catalysts over the surface of a photocatalyst under stirring movement. As shown in Figure 16b, the nanoparticle formation mechanism in this technique can be divided in four steps: (i) discrete nucleation of atoms and atomic clusters on the powder surface. (ii) Growth of islands that acquire very slow nucleation and growth kinetics due to the constant stirring movement of the support. This process inhibits coalescence, thereby preventing the formation of thin films. (iii) Aggregation of adjacent islands and (iv) subsequent formation of nanoparticles.[82]

2 MATERIALS AND METHODS

2.1 Materials and Reagents

Commercial reagents employed in this work were used as received, without any purification procedure. The production of the photocatalysts $NaTaO_3$ and Bi-doped $NaTaO_3$ involved tantalum pentoxide (Ta_2O_5) (Alfa Aesar, 99.9%), sodium carbonate (Na_2CO_3) (Merck, 99.5%), sodium chloride (NaCl) (Merck, 99.5%), Bismuth Oxide (Bi_2O_3) (Alfa Aesar, 99.5%) and Bismuth nitrate pentahydrate ($Bi(NO_3)_3{:}5H_2O$) (Mallinckrodt, 99.9%).

Moreover, magnetron sputtering deposition of Ni nanoparticles has been conducted with a 2-inch target consisting of Ni (Process Materials, 99.99%).

2.2 Molten salt synthesis of $NaTaO_3$

For the production of 1g of $NaTaO_3$, Ta_2O_5, Na_2CO_3 and NaCl were mixed for 1 hour in a mortar with Na_2CO_3 : Ta_2O_5 : NaCl molar ratios of 1 : 1 : 2.5. The powder was taken to a furnace at 820-1000 °C for 5 h using a heating rate of 3 °C/min and room temperature cooling. In order to remove NaCl, the product was repeatedly washed and centrifuged with deionized water, and finally dried at 80 °C during 12 h for obtaining $NaTaO_3$ powder. These steps are illustrated in Figure 17.

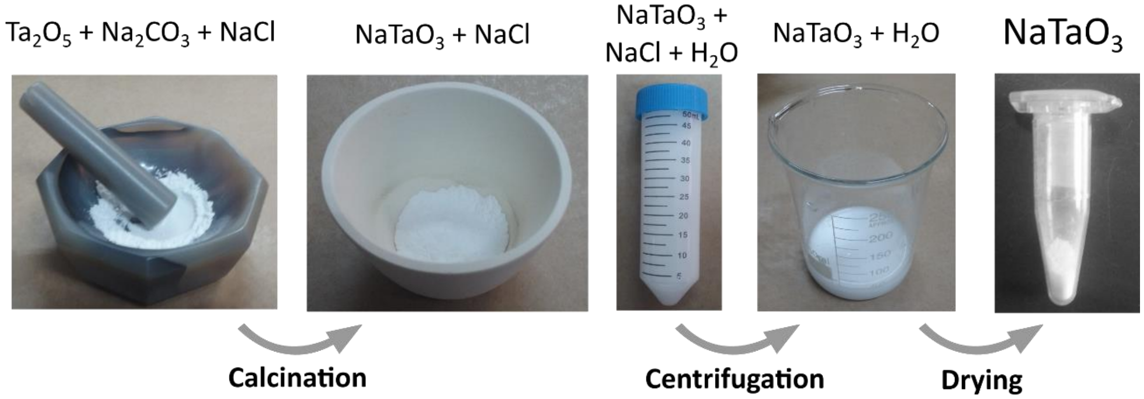

Figure 17 – Main steps of the molten salt synthesis, showing the compounds that are present in each stage
Source: By the author

2.3 Molten salt synthesis of Bi-doped $NaTaO_3$

Bi-doped $NaTaO_3$ was obtained by following a similar procedure as for pure $NaTaO_3$. In the initial synthesis step, the bismuth precursor $Bi(NO_3)_3{:}5H_2O$ was mixed with the other reactants using Na_2CO_3 : Ta_2O_5 : $Bi(NO_3)_3$: NaCl molar ratios of 1 : 1-X : X : 2.5, while the dopant concentration (X) was varied from 0.5 to 5 mol%. The subsequent steps of calcination at 1000 °C for 5 h, centrifugation and drying remained identical to those employed for $NaTaO_3$. Alternatively, Bi-doped $NaTaO_3$ was also produced at 820°C and with Bi_2O_3 as the Bi precursor.

2.4 Cocatalyst deposition

Cocatalysts were deposited by magnetron sputtering over 200 mg samples of 3 mol% Bi-doped $NaTaO_3$, at a DC power of 150 W from 5 to 20 minutes with a 15 sccm Ar flow. A powder stirring device consisting of a glass container and a loudspeaker set at approximately 80 Hz was employed in order to promote homogeneous distribution of material during the nanoparticle deposition, as illustrated in Figure 18. The distance between the substrate and the target was 5 cm. Prior to the deposition procedure, the sputtering chamber was evacuated until a base pressure of 10^{-6} Torr was established.

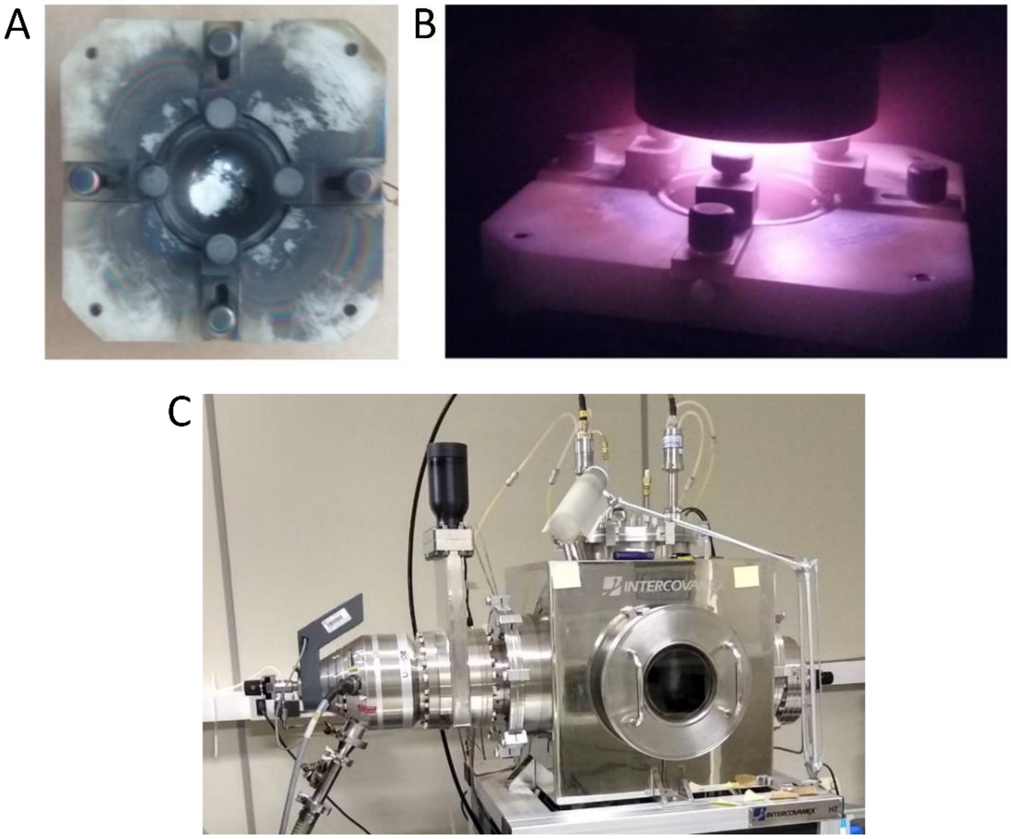

Figure 18 – Top view of the powder stirrer (a), formation of the argon plasma during sputtering deposition on the powder substrate (b) and the vacuum chamber that contains the sputtering setup (c)
Source: By the author

2.5 Material characterization

In order to investigate the structural properties of $NaTaO_3$ and Bi-doped $NaTaO_3$, Raman spectroscopy (*Renishaw RM2000*, 632.8 nm laser) and X-ray diffraction with silicon powder as a reference for calibration (*Rikagu Ultima IV* diffractometer, Cu Kα source) were conducted. Crystallinity and elemental composition were further evaluated by high-resolution transmission electron microscopy (HRTEM) (*Double Aberration-Corrected Titan Cubed Themis*, *Ceta S CMOS* camera) and Energy-Dispersive X-ray Spectroscopy (EDS) (*Super XG1* detector). Optical properties were investigated through Diffuse Reflectance UV-Vis spectroscopy (*Shimadzu UV-2600*).

Surface morphology was analysed by Scanning electron microscopy (*ZEISS FEG Sigma Gemini*) and surface composition was analyzed by X-ray photoelectron spectroscopy (*Scienta-Omicron ESCA+*, Al Kα source), using a low energy electron flood gun for charge compensation. Considering the binding energy of adventitious carbon (C-C at 284.8 eV), XPS spectra were calibrated and data analysis was performed using the *CasaXPS* software, with a Voigt function applied for peak fitting.

2.6 Photocatalytic hydrogen evolution

Photocatalytic reactions were carried out in a 90 mL quartz reactor, using argon (99.999%) with a 0.9 mL/min constant flow as a carrier gas. Prior to the photocatalytic reactions, residual gases in the reactor were extracted by repeatedly evacuating and purging with argon. A 300 W Xe lamp was used as the light source and the irradiation power density was measured and calibrated (*Gentec XLP 12-3S-H2-D0* photometer) by adjusting the distance between the lamp and the reactor. A water column filter was connected directly to the lamp system in order to block infrared radiation, and an AM 1.5G filter was used as a solar simulator. Accordingly, Figure 19a illustrates the arrangement of these components for the photocatalytic reactions.

The reactor system is connected to a gas chromatograph (*Agilent 7890B*), which automatically performs periodic gas injections and subsequently provides the quantification of the evolved volumes of H_2 and O_2. The chromatograph was calibrated with 10 µL gas syringes for a precise detection of micro molar amounts of gas.

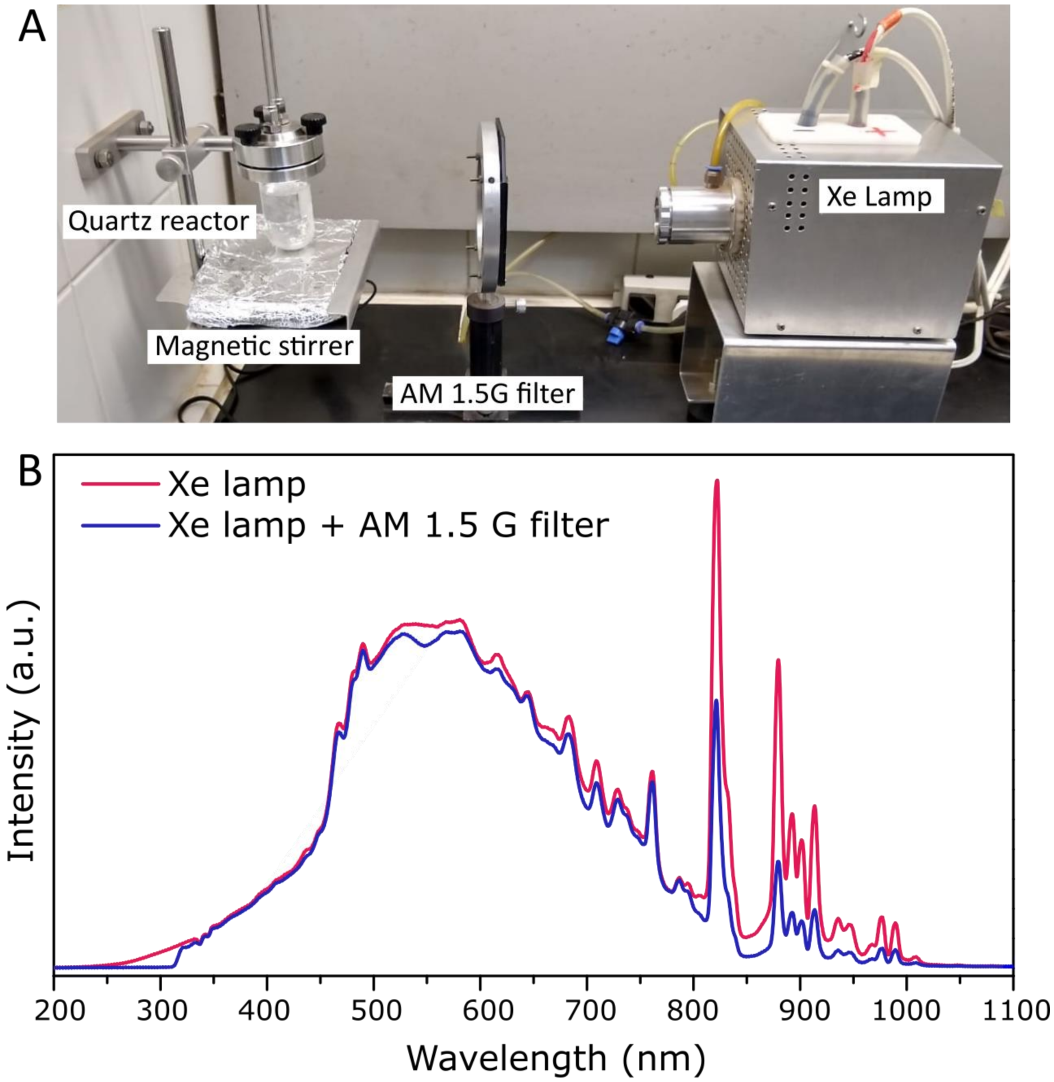

Figure 19 – Experimental setting for the photocatalytic water splitting reactions under simulated sunlight (a), Irradiation spectrum of the two systems employed as light sources in the work: The Xe lamp (red) and the Xe lamp + AM 1.5G system (blue) (b)

Source: By the author

Hydrogen evolution with $NaTaO_3$ photocatalysts was conducted under 300 mW/cm^2 irradiation, without the AM 1.5G filter. Powder photocatalysts (25 mg) were dispersed in an ultrasonic bath for 15 min, following suspension in a 50 mL solution composed of methanol (20 vol%) and deionized water, under stirring movement.

Photocatalytic hydrogen evolution with Bi-doped $NaTaO_3$ and Bi-doped $NaTaO_3$/Ni was evaluated under 300 mW/cm^2, using the AM 1.5G filter to simulate the solar spectrum, which is illustrated in Figure 19b. Powder photocatalysts (25 mg) were dispersed in an ultrasonic bath for 15 min, following suspension in a 50 mL solution composed of methanol (20 vol%) and deionized water, under stirring movement.

3 RESULTS

3.1 Production of pure $NaTaO_3$

In order to obtain a single-phase particulate photocatalyst with an adequate morphology for the water splitting reaction, $NaTaO_3$ powder was produced through the molten salt method, following a previously reported procedure. [42] The synthesis was carried out under varied calcination temperatures, while keeping a fixed molar ratio between the reactants and NaCl. The temperature range between 820°C and 1050°C was established considering that NaCl melts at 800°C and the upper limit of the utilized furnace is 1050°C.

The crystal structure of each sample was investigated via X-ray diffraction (XRD). The data in Figure 20 confirm the formation of $NaTaO_3$ in the orthorhombic perovskite phase (space group *Pcmn*), considering the reference pattern for the compound (ICSD 23319). [9] The similar width of the diffraction peaks indicate that calcination temperature has little influence in the crystallite size of $NaTaO_3$ produced between 820°C and 1050°C. Furthermore, the results show the absence of any abundant second phase or possible residual phases such as NaCl and Ta_2O_5, as all features in the XRD pattern can be ascribed to orthorhombic sodium tantalate.

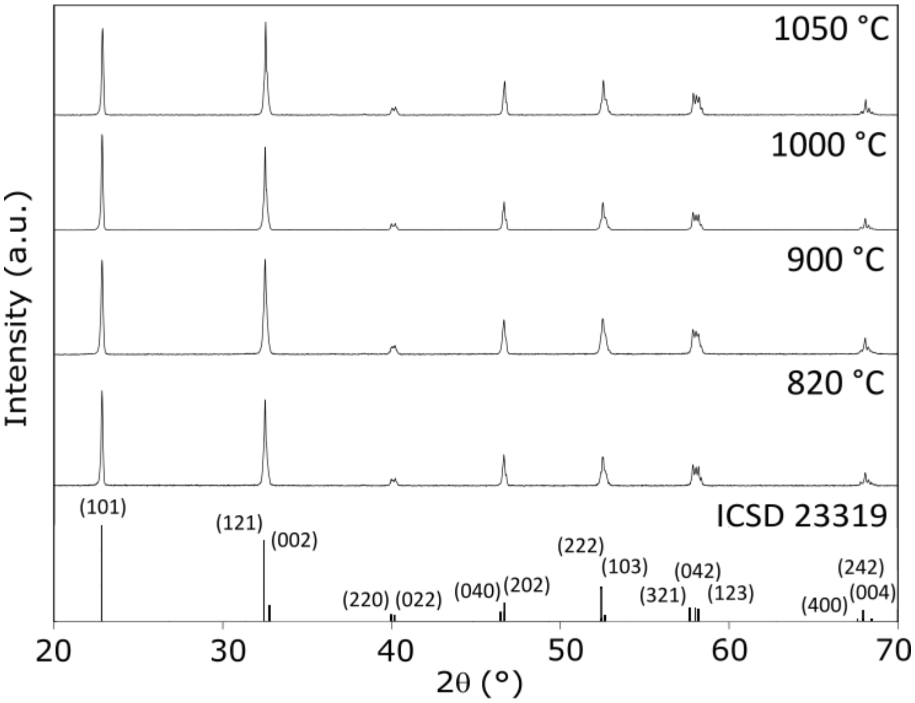

Figure 20 – X-Ray diffraction patterns of $NaTaO_3$ obtained by the molten salt method under different temperatures, in comparison with reference data for orthorhombic $NaTaO_3$

Source: By the author

The morphology of the $NaTaO_3$ samples obtained at varied temperatures was investigated by Scanning Electron Microscopy (SEM), as shown in Figure 21. As an expected result of the molten salt method, the observed particles exhibit perpendicular and well-defined facets, which may be beneficial for photocatalytic applications, since this cubic morphology may provide exposed facets for the deposition of co-catalysts and the production of heterojunctions. Although the XRD patterns do not show significant variation in terms of crystallinity, the calcination temperature is shown to exert expressive influence on particle morphology. As higher temperatures may provide additional energy for crystal growth, the average size of the particles is roughly proportional to the calcination temperature.

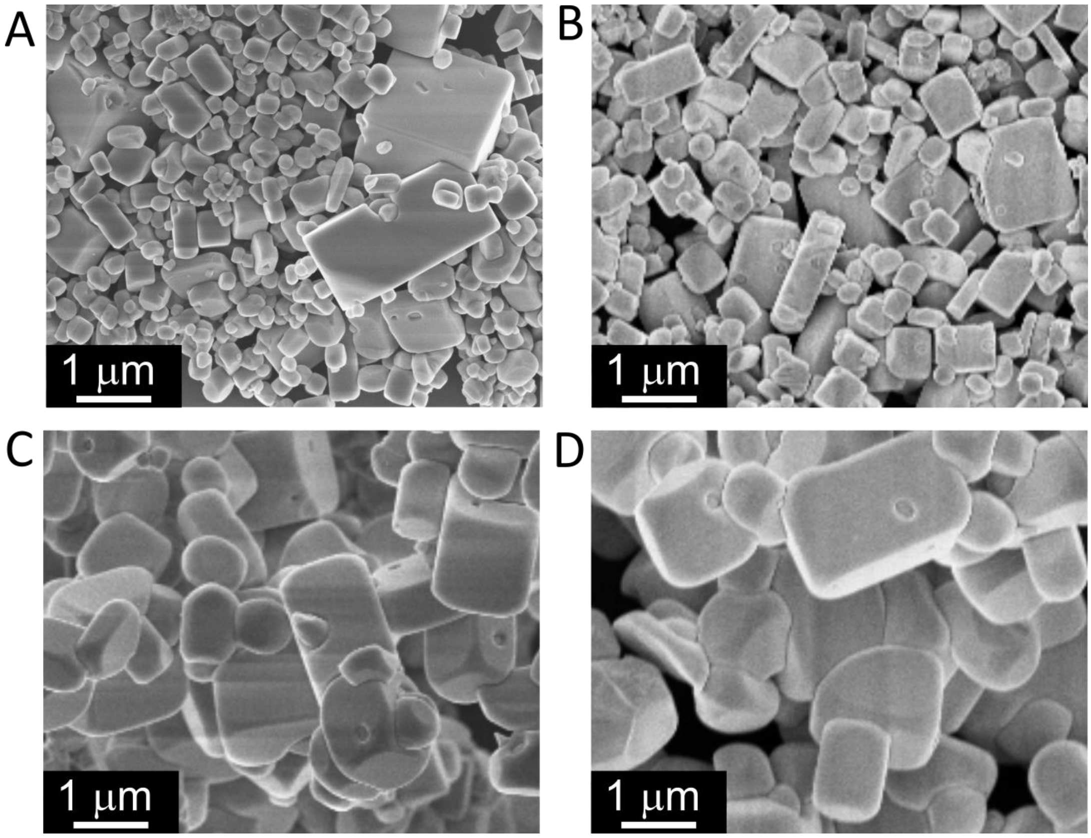

Figure 21 - SEM images of NaTaO3 obtained under 820 ºC (a), 900 ºC (b) 1000 ºC (c) and 1050 ºC (d)
Source: By the author

Subsequently, in order to quantify the surface area for the $NaTaO_3$ samples, the samples were analysed through the BET method. Accordingly, the data in Figure 22 show that this value increases sharply for lower calcination temperatures, as these conditions result in the smallest particles, in a consistent manner with the pattern suggested by SEM data.

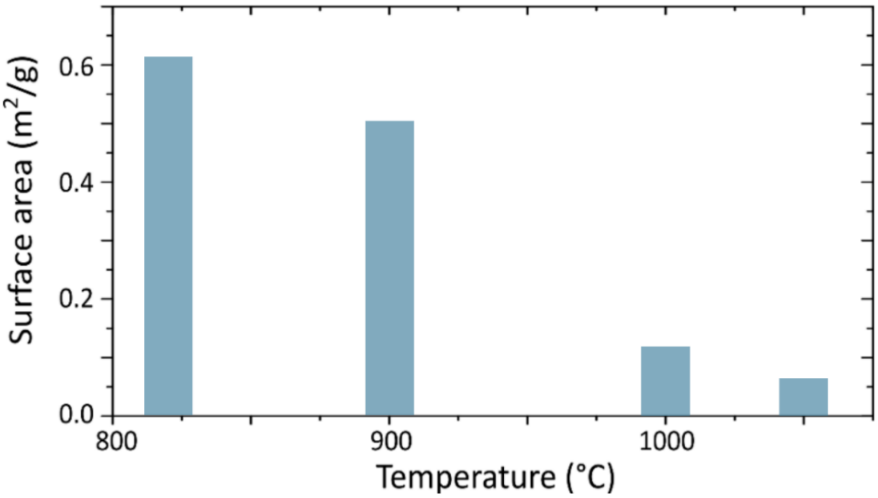

Figure 22- Surface area of $NaTaO_3$ samples produced at different temperatures, measured by multimolecular adsorption (BET method)

Source: By the author

Seeking to verify the influence of calcination temperature in the photocatalytic activity of $NaTaO_3$, hydrogen evolution in a suspension system with methanol was evaluated for 5h by gas chromatography, as shown in Figure 23. As expected, the material exhibits stable photocatalytic activity and considerable rates of H_2 production when the Xe lamp is used as the light source, while the activity is negligible when the AM 1.5G filter is connected to the lamp. Consistently with the wide band gap of $NaTaO_3$, this demonstrates the system only presents hydrogen evolution due to the absorption of UV light, since the solar simulator filter blocks the spectrum with photon energy approximately above 3.8 eV.

Among these samples, $NaTaO_3$ obtained at 820 ºC is by far the most efficient photocatalyst for water splitting, producing 77.9 μmol/h of H_2 under these conditions. The material produced at 1050, 1000 and 900° C exhibit hydrogen evolution rates of 3.7, 5.7 and 9.0 μmol/h, respectively. This trend may be partially associated to the increased area for surface redox reactions in samples produced at lower temperatures, as evidenced by the BET data in Figure 22. However, the striking disparity between the H_2 evolution rates in the 900° C and 820 ºC samples may be a consequence of another factor, since they are comparable in terms of surface area, morphology, and crystallinity.

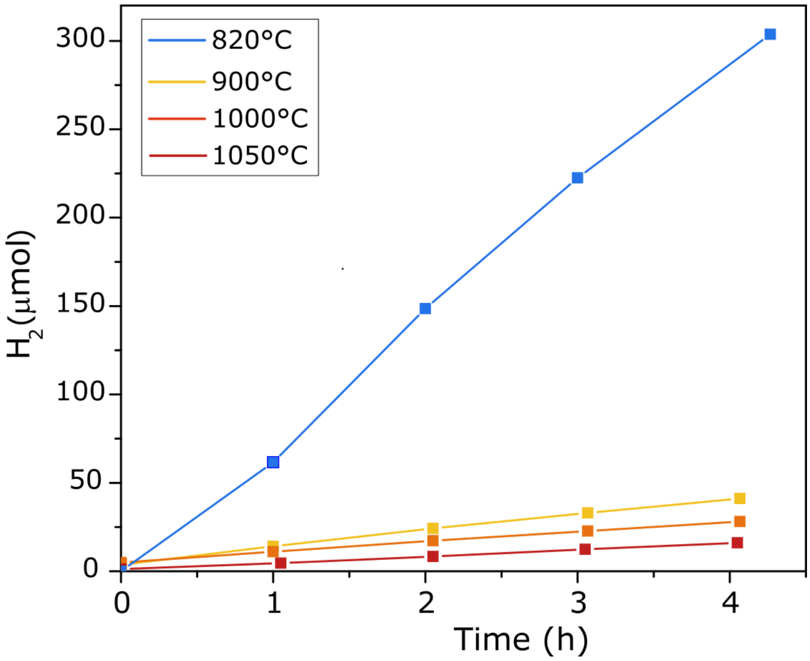

Figure 23 – Hydrogen evolution in H2O + 20 vol% CH3OH for 25mg of $NaTaO_3$ produced at different temperatures, using a Xe 300W lamp with 300 mW/cm2 power density.
Source: By the author

In order to better understand the reasons for the high photocatalytic activity of $NaTaO_3$ produced at 820 °C, UV-vis spectroscopy was performed, as shown in Figure 24a. Consistently with the expected band gap of 4 eV, the material produced at the lowest temperature exhibits a steep absorption edge situated between 300 and 320 nm, similarly as typically reported for $NaTaO_3$.[84] In addition to this main band, $NaTaO_3$ produced at higher temperatures presents a secondary absorption edge at longer wavelengths. This feature indicates the presence of electronic transitions that are narrower than the band gap, as a possible effect of a different defect chemistry.

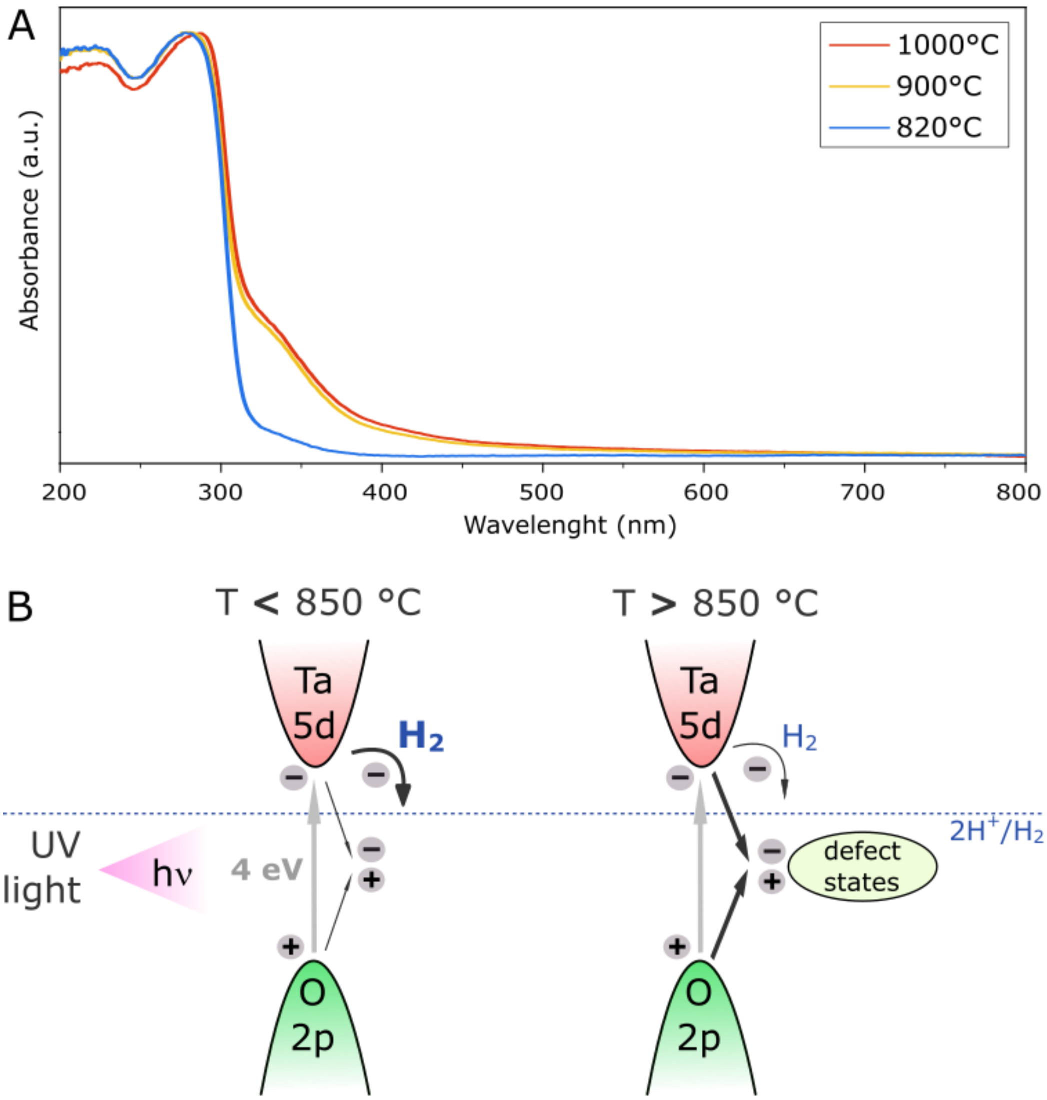

Figure 24 – UV-vis spectrum of $NaTaO_3$ obtained at varied temperatures, (a) suggested mechanism for the higher photocatalytic activity of $NaTaO_3$ produced at 820 °C (b)
Source: By the author

The remarkable difference between the optical absorption bands in Figure 24a may be closely associated with the volatilization of the sodium precursor Na_2CO_3 during the calcination procedure of the molten salt synthesis. As Na_2CO_3 melts at 850 °C, a small percentage of this compound may volatilize at higher temperatures, [85] thereby leading to Na-deficiency in $NaTaO_3$ produced above 850°C. Therefore, as illustrated in Figure 24b, structural defects could introduce electronic states that are detected in the optical absorption spectra, although they may lead to increased recombination rates, as photocatalytic activity is lower when this feature is present. Similarly, previous studies have demonstrated that the addition of a 5% excess of

Na_2CO_3 is able to greatly enhance the photocatalytic activity of $NaTaO_3$,[84] even though a detailed explanation of this effect has not been proposed so far.

3.2 The influence of Bi doping on $NaTaO_3$

Given the wide band gap of pure $NaTaO_3$, Bi doping has been recently proposed as a method to introduce midgap electron states that may promote photocatalytic activity under visible and near-UV irradiation. However, most studies have focused on dopant concentrations above 5 mol%, while lower values have remained unexplored. In order to further investigate the effect of this dopant in $NaTaO_3$, Bi-doped sodium tantalate was obtained by introducing a Bi precursor along with TaO_5, Na_2CO_3 and NaCl at the first step of the molten salt synthesis. Accordingly, bismuth trioxide (Bi_2O_3) and bismuth nitrate pentahydrate ($Bi(NO_3)_3.5H_2O$) were initially tested at 820 ºC and 1000 ºC calcination temperatures, using a 5% Bi/Ta molar ratio, in order to determine the most suitable conditions for the doping process.

Considering that Bi-doped $NaTaO_3$ has been previously reported to be active under visible light, the photocatalytic reaction was now executed with the AM 1.5G filter, which acts as a solar simulator. As expected, hydrogen evolution under solar-simulated irradiation is negligible for pristine $NaTaO_3$, while most 5% Bi samples exhibit considerable photocatalytic activity, as shown in Figure 25. The calcination temperature of 1000 ºC results in more active materials in comparison to 820 ºC, most likely due to the improved kinetics for the assimilation of Bi atoms into the $NaTaO_3$ lattice. Furthermore, samples produced with $Bi(NO_3)_3$ exhibit higher H_2 evolution rates, as this precursor may present better reactivity than the more stable bismuth trioxide.

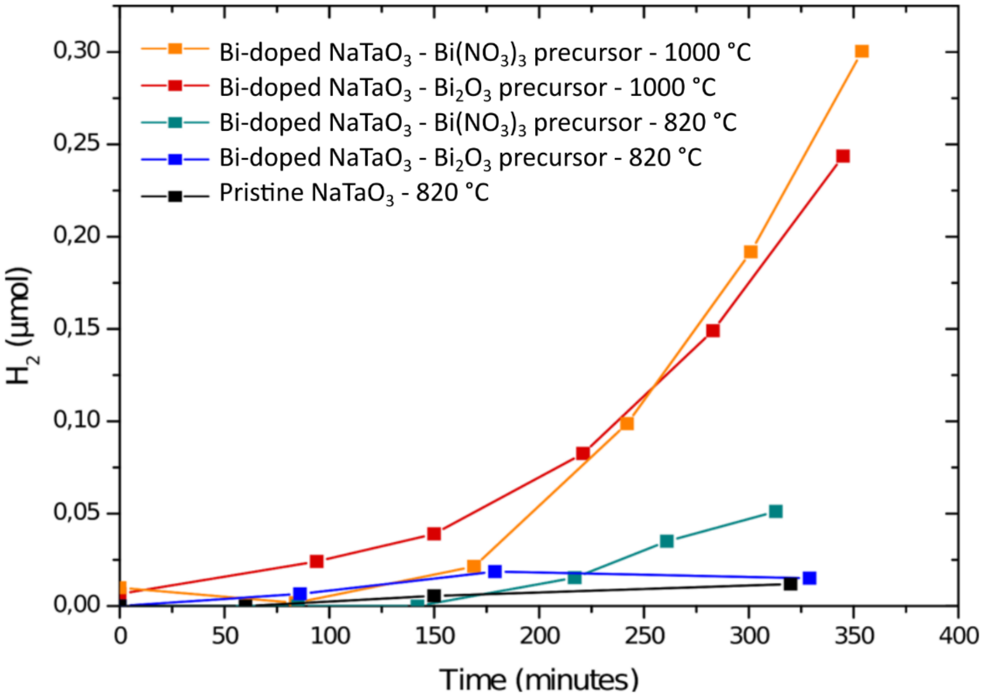

Figure 25 - Hydrogen evolution in H_2O + 20 vol% CH_3OH for 25mg of 5 mol% Bi-doped $NaTaO_3$ using the AM 1.5G solar simulator filter, with a Xe 300W lamp at a power density of 300 mW/cm^2
Source: By the author

After the 6h photocatalytic reaction, all the 5% Bi-doped samples exhibit a dark grey color, in contrast with their initial white aspect, as shown in Figure 26a. Since this effect is not observed when pristine $NaTaO_3$ undergoes irradiation, the result suggests that secondary phases may be present, in addition to Bi-doped $NaTaO_3$. Correspondingly, Figure 26b shows that X-ray Photoelectron (XPS) spectra exhibit an exceedingly high concentration of surface Bi with respect to Ta atoms, a fact that strongly indicates surface segregation of bismuth species. These features suggest that a fraction of Bi atoms from the precursor may not have been introduced into the $NaTaO_3$ lattice, thus giving rise to Bi_2O_3 particles after annealing in ambient air. Subsequently, Bi_2O_3 is able to react with CO_2 diluted in water in the presence of light, which allows the formation of bismuth subcarbonate ($Bi_2(CO_3)_3$) during the photocatalytic reaction, similarly as reported in other studies. [86]

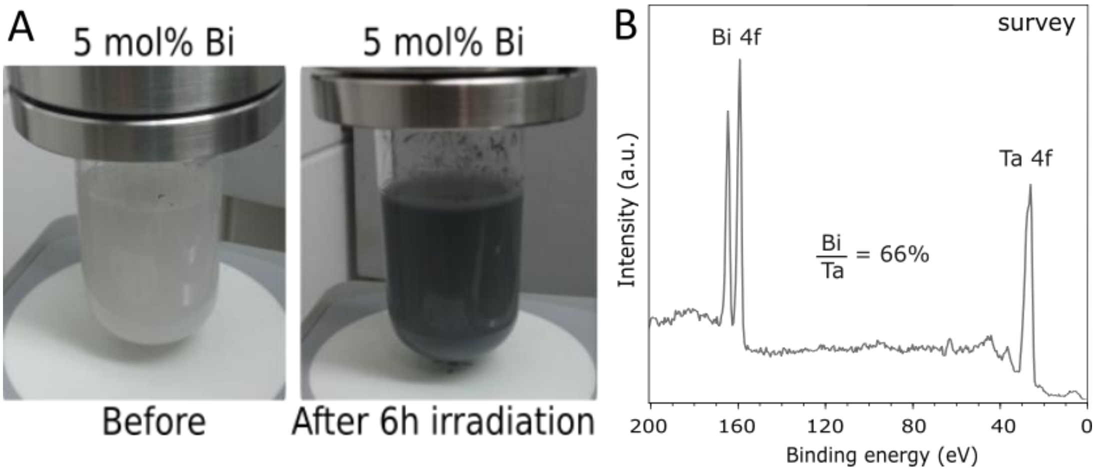

Figure 26 – Quartz reactor with H_2O, methanol and 25 mg of 5 mol% Bi-doped $NaTaO_3$, before and after AM 1.5G irradiation (a) and selected region in the wide scan XPS spectrum of 5 mol% Bi-doped $NaTaO_3$, showing the calculated surface atomic ratio between Bi and Ta (b)
Source: By the author

In order to further investigate the effect of Bi doping on the structure and photocatalytic properties of $NaTaO_3$, the same synthesis procedure was carried out using lower bismuth concentrations. In this manner, the formation of surface Bi_2O_3 may be avoided and the Bi-doped structure can be more adequately characterized. Since the highest hydrogen evolution rates for 5 mol% Bi samples were achieved by employing the calcination temperature of 1000 ºC and $Bi(NO_3)_3$ as the bismuth precursor, these synthesis conditions were chosen for the production of 0.5, 1, 2, 3 and 4 mol% Bi-doped $NaTaO_3$.

In contrast with the micro-cubic morphology observed for pristine $NaTaO_3$, Bi-doped samples are composed of significantly smaller particles, as demonstrated by the SEM images in Figure 27. In a similar manner for all samples, doping from 0.5 to 5 mol% produces nanocubes with well-defined facets. The surface reconstruction suggests the dopant may induce structural modification, and the greater surface area in the doped material can be regarded as a beneficial property for photocatalytic applications.

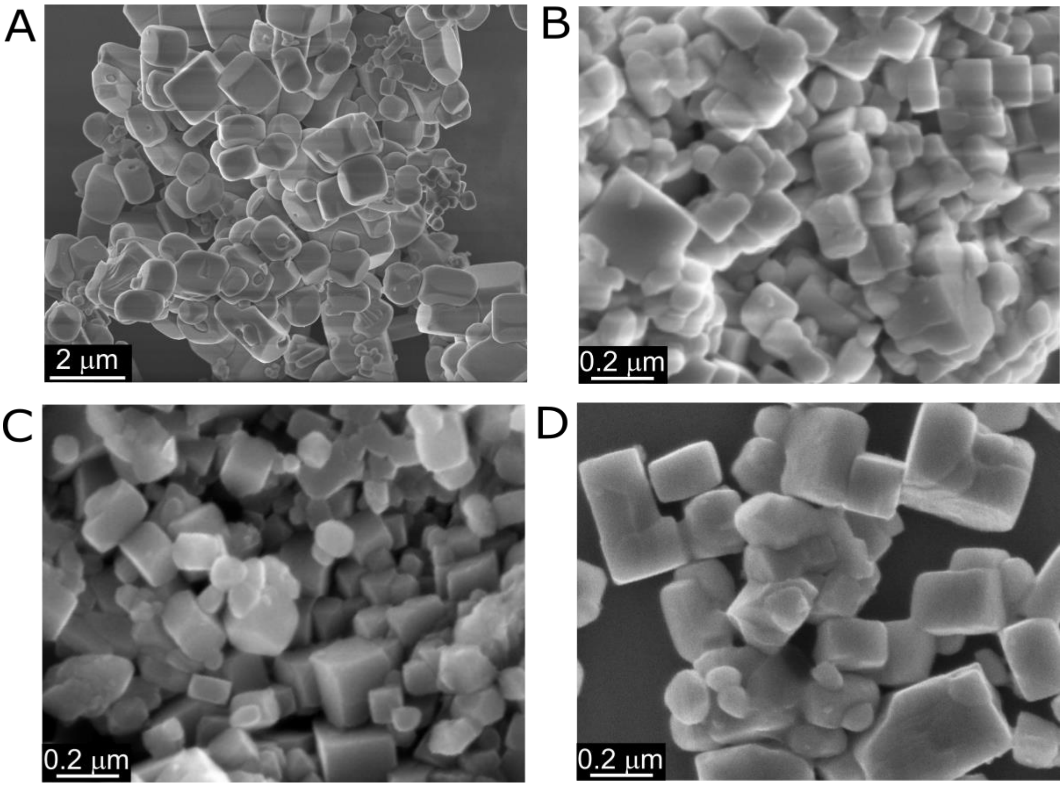

Figure 27 – SEM images of pristine (a) and Bi-doped $NaTaO_3$ with 0.5 (b), 3 (c) and 5 (d) mol% Bi
Source: By the author

Furthermore, High-Resolution Transmission Electron Microscopy (HRTEM) images in Figure 28 give evidence of the characteristic (110) plane in 3 mol% Bi-doped $NaTaO_3$, showing the interplanar spacing of 0.274 nm, similarly as previously reported for the material. [87]

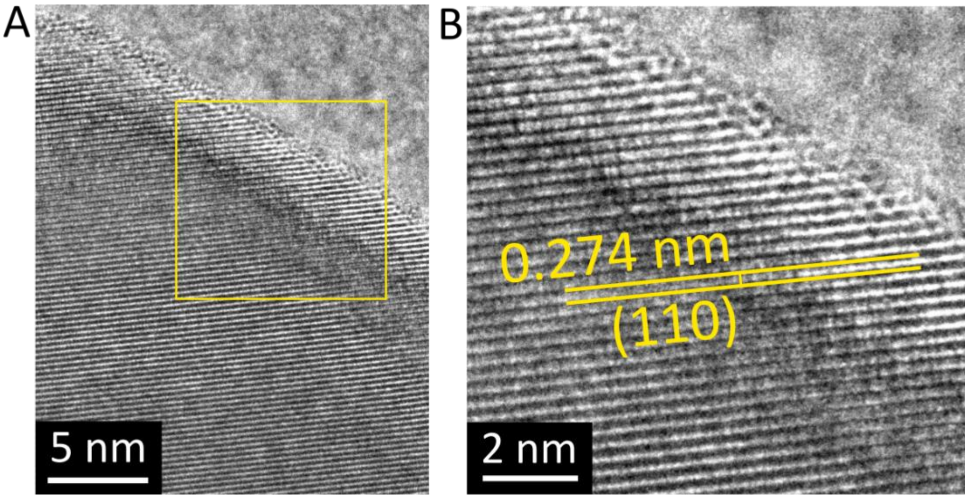

Figure 28 – TEM image of 3 mol% Bi-doped $NaTaO_3$, (a) showing a magnified view of the region in the yellow square (b)
Source: By the author

A clear evidence of the structural influence of Bi-doping in the perovskite lattice is provided by the comparison between the X-ray diffraction patterns of Bi-doped $NaTaO_3$ and the pristine material, as shown in Figure 29. Although the wide scan in Figure 29a shows a similar profile for all samples, a detailed inspection of some peaks reveals some clear effects of Bi doping on the crystalline structure of $NaTaO_3$. Highlighting the most intense peak in the diffraction pattern, Figure 29b shows that the addition of Bi at low concentrations induces a subtle lattice expansion, as the peak may be shifted to lower angles as a result of Bi doping. In view of the ionic radii of Bi^{3+} (103 pm), Na^{+} (102 pm) and Ta^{5+} (64 pm), this feature suggests Bi doping takes place in the Ta site, although it does not rule out substitution in both sites.[61]

A major effect of Bi doping on the structure of $NaTaO_3$ is observed between 0.5 mol% to 4 mol% Bi, as these samples do not exhibit the same sub-peak pattern of pristine $NaTaO_3$ in the region of 40°, 58° and 68°, as indicated in Figure 29c. This remarkable difference suggests the formation of a pseudocubic perovskite from 0.5 to 4 mol% Bi-doped $NaTaO_3$, while 5 mol% Bi-doped $NaTaO_3$ presents a transition to the orthorhombic phase.[88] In correspondence with previous studies, the observed profile between 0.5 mol% to 4 mol% Bi doping is an evidence of a perovskite phase with closely similar a, b and c lattice parameters, [51,89] even though the present data may not allow for an accurate determination of the crystal structure. Therefore, this feature is coherent with the pseudocubic Cmcm phase that had been previously observed at room temperature due to the introduction of K, Ca and Ti dopants in $NaTaO_3$,[50] as well as the monoclinic structure obtained by the sol-gel synthesis, which presents a monoclinic angle close to 90°. Moreover, the partially-split XRD pattern reveal that the orthorhombic lattice arises again in 5 mol% Bi-doped $NaTaO_3$, although the pseudocubic phase may still be present as a minor contribution.

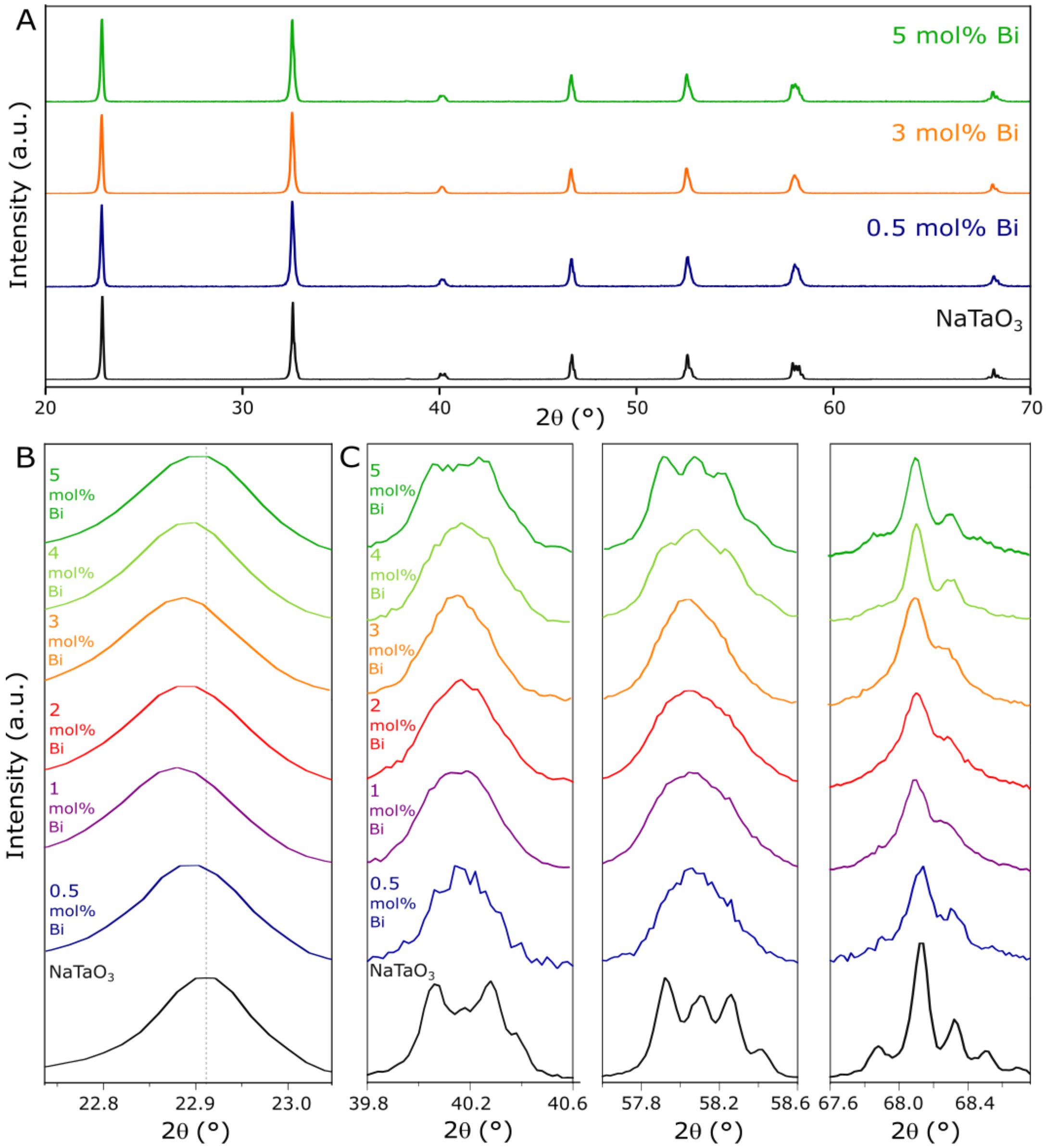

Figure 29 - X-ray diffraction patterns from pristine and Bi-doped $NaTaO_3$, showing wide scan profiles (a), the effect of doping on lattice expansion (b) and the different sub-peak pattern in orthorhombic and pseudocubic perovskite lattices (c)

Source: By the author

A strong indicator of Bi-Ta substitution is provided by Raman spectroscopy, as shown in Figure 30. The only remarkable difference between the Raman spectra of pristine and Bi-doped $NaTaO_3$ is the highlighted band located at 863 cm^{-1}, which can be associated to the A_{1g} breathing mode of TaO_6 octahedrons. As the symmetry of pristine perovskites forbids this vibrational mode, its presence suggests broken symmetry due to Ta-site atomic substitutions, similarly as previously reported for other dopants. [90-91] Given the sharp difference between the ionic radii of Bi^{3+} (103 pm) and Ta^{5+} (64 pm), lattice distortion due to the Bi-Ta substitution might be one of the reasons for the structural transition observed in XRD patterns. Furthermore, the distinct oxidation states of these ions may also induce the formation of other defects as a charge compensation mechanism, which may involve Bi^{3+}- Na^{+} doping or atomic vacancies at O^{2-} and sites.

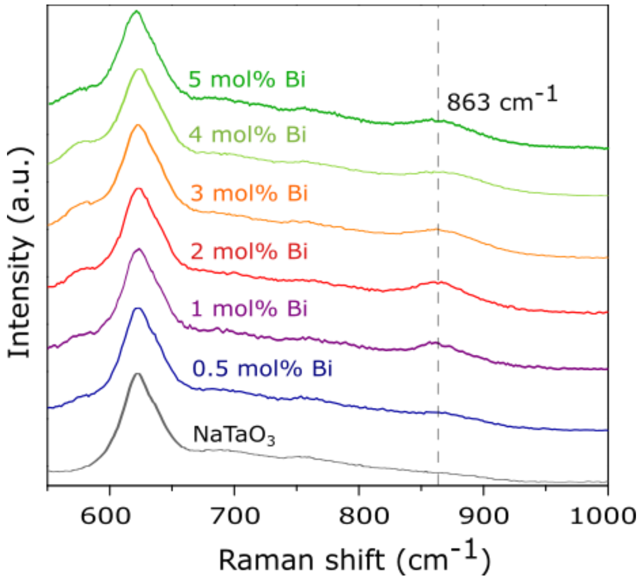

Figure 30 - Raman scattering spectra of pristine and Bi-doped $NaTaO_3$, highlighting the band related to the A_{1g} vibrational mode, at approximately 863 cm^{-1}.

Source: By the author

The surface chemical composition of the material was examined by X-ray photoelectron spectroscopy (XPS). Accordingly, high-resolution XPS spectra of Bi-doped and pristine $NaTaO_3$ are shown in Figure 31a and 31b, respectively. As expected, the energy of Ta 4f doublets refer to Ta^{5+} species, which are present in the form of Ta_2O_5 (26.6 and 28.5 eV) and $NaTaO_3$ (25.5 and 27.4 eV) in both samples. [92-93] The significant presence of surface Ta_2O_5 can be attributed to the volatilization of the Na precursor Na_2CO_3 during calcination at 1000ºC. Nevertheless, the amount of tantalum oxide is too low to be detected by bulk characterization techniques, such as XRD and UV-vis spectroscopy.

The region related to O 1s shows four contributions from O^{2-} in both samples. The most significant contribution at 529.7 eV consists of metal-bonded oxygen in the lattices of $NaTaO_3$ and Ta_2O_5. The secondary peaks at higher energies can be ascribed to oxygen vacancies in the crystal lattice (531,1 eV), OH^- from adsorbed H_2O species (532.3 eV) and molecular water (533.7 eV), although adsorbed organic contaminants could also contribute in this region. [94-96] In contrast with pristine $NaTaO_3$, 3 mol% Bi-doped samples exhibits a lower intensity in the peak related to V_O, as oxygen vacancies may become more prominent due to doping. In correspondence with the Raman spectroscopy results, these defects may arise as part of a charge compensation effect induced by Bi^{3+}-Ta^{5+} atomic substitutions.

The Bi 4f doublet (159.1 and 164.5 eV) indicates that the dopant is present in the Bi^{3+} chemical state, as the employed precursor $Bi(NO_3)_3.5H_2O$ consists of this species. The spectrum presents a low intensity when compared to the other elements, and its energy could be associated to Bi in the $NaTaO_3$ lattice, as well as surface Bi_2O_3 to a lower extent, [97] as well as some minor contribution of Bi_2O_3. [98]

The surface concentration of each element in Bi-doped and pristine $NaTaO_3$ samples was evaluated by a combined quantification of survey and high-resolution XPS spectra, considering only the contributions from O and Ta that are inherent to the $NaTaO_3$ lattice. Since the surface concentration of Ta remains similar in all samples, the quantification of the other elements was reported in the form of Na/Ta, O/Ta and Bi/Ta ratios, as shown in Figure 31c. As expected, pristine $NaTaO_3$ presents a Na:Ta:O surface ratio close to the ideal value of 1:1:3, even though some sodium vacancies may be present as a result of Na_2CO_3 volatilization during the calcination procedure. When the dopant is introduced in $NaTaO_3$ at 0.5 mol%, the concentration of lattice oxygen is sharply diminished, and remains similarly low for higher Bi concentrations, thus indicating the presence of oxygen vacancies in the doped surface. This effect might be one of the factors behind the altered morphology of Bi-doped samples, [99] and it could play a significant role in photocatalytic reactions, as surface oxygen atoms are directly involved in the adsorption of H_2O molecules. [100] Moreover, increased amounts of Bi may also promote superficial Na vacancies, coherently with the Na^+-Bi^{3+} substitutions, which are likely to occur, given the similarity between the atomic radii of these cations. Finally, the proportion of surface Bi is shown to rise gradually below 4 mol% doping, but a strong increase occurs in the 5 mol% Bi sample. This pattern suggests that a fraction of bismuth may be segregated at the surface in the form of Bi_2O_3, as discussed in Figure 26. This distinct effect due to high-concentration doping can be correlated with the structural transition between 4 and 5 mol% observed in the XRD results, which indicates that the pseudocubic regime reaches a threshold at this point, and the $NaTaO_3$ lattice no longer accommodates the dopant at higher Bi concentration.

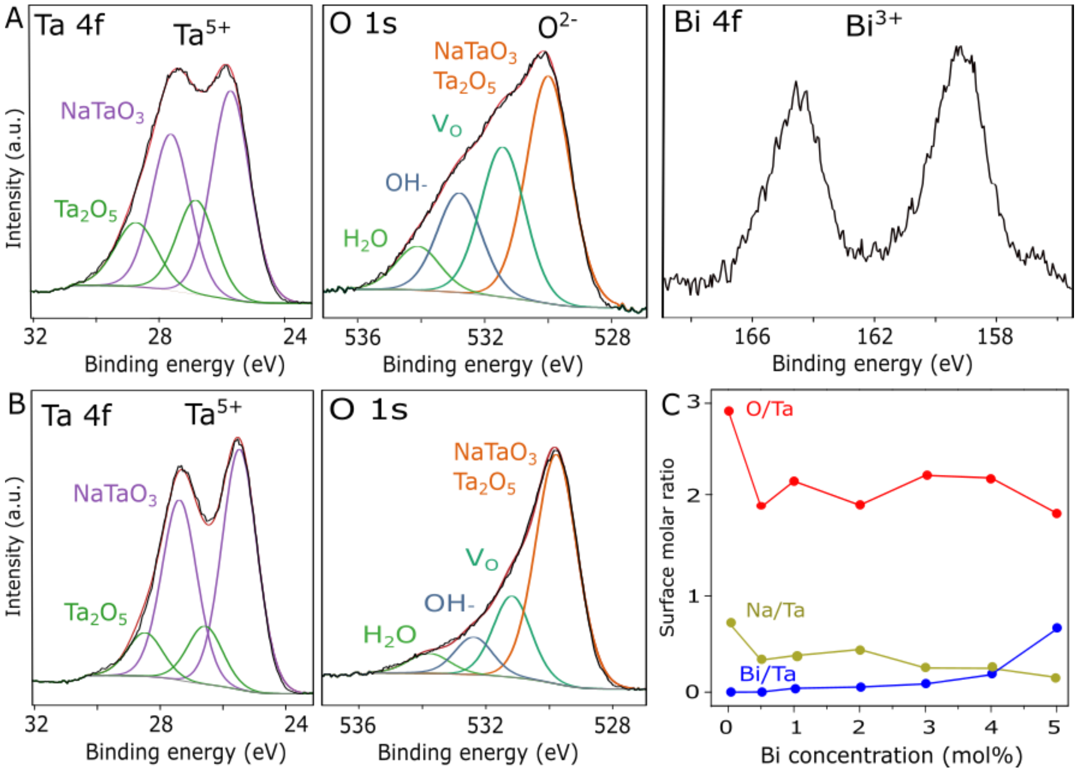

Figure 31 - High-resolution X-ray photoelectron spectra of 3 mol% Bi-doped $NaTaO_3$ (a), pristine NaTaO3 (b) and surface composition of the material, determined by XPS (c)
Source: By the author

Previous studies have suggested that the stabilization of the pseudocubic phase of $NaTaO_3$ may be directly associated with low-temperature (<600ºC) synthesis conditions.[51] Here, however, Bi-doped $NaTaO_3$ was obtained at 1000ºC, which indicates that this factor may not fully explain the structural transition. A plausible hypothesis is that the abundance of structural defects, such as Na and O vacancies may play a key role in the formation of this pseudocubic phase. Accordingly, previously reported low-temperature procedures could have led to a defect-rich $NaTaO_3$ lattice, which in turn allowed the formation of the pseudocubic phase. Nonetheless, further studies are necessary in order to elucidate the influence of the defect chemistry on the orthorhombic-pseudocubic transition.

$NaTaO_3$ typically presents a wide band gap around 4 eV, which only allows absorption of a negligible fraction of ultraviolet light from the solar spectrum. In Figure 32a, UV-vis spectroscopy data reveal that Bi-doped $NaTaO_3$ can also absorb less energetic photons as Bi is introduced in the perovskite lattice. In virtue of the structural defects discussed in Figure 24, the sample doped with 0.5 mol% Bi exhibits a broader absorption band with respect to other samples, similarly as in pristine $NaTaO_3$. Nevertheless, as the dopant concentration increases, the formation of these defects may be attenuated, and band-gap narrowing takes place, as demonstrated by the Tauc plots in Figure 32b. Due to its pseudocubic structure, Bi-doped samples with low Bi concentrations feature an indirect band gap (r = 2), while the orthorhombic/pseudocubic 5 mol% Bi-doped material presents an additional direct band gap (r = ½). The narrowed band gap indicates that Bi-doped $NaTaO_3$ is able to absorb UV light from the solar spectrum (see the AM 1.5G spectrum in Figure 19), thereby allowing photocatalytic application under solar-simulated irradiation. In previous theoretical studies, Bi-doping has been shown to promote Bi 2s midgap states in virtue of Bi-Ta atomic substitutions, [61] correspondingly with the experimental results achieved in this work.

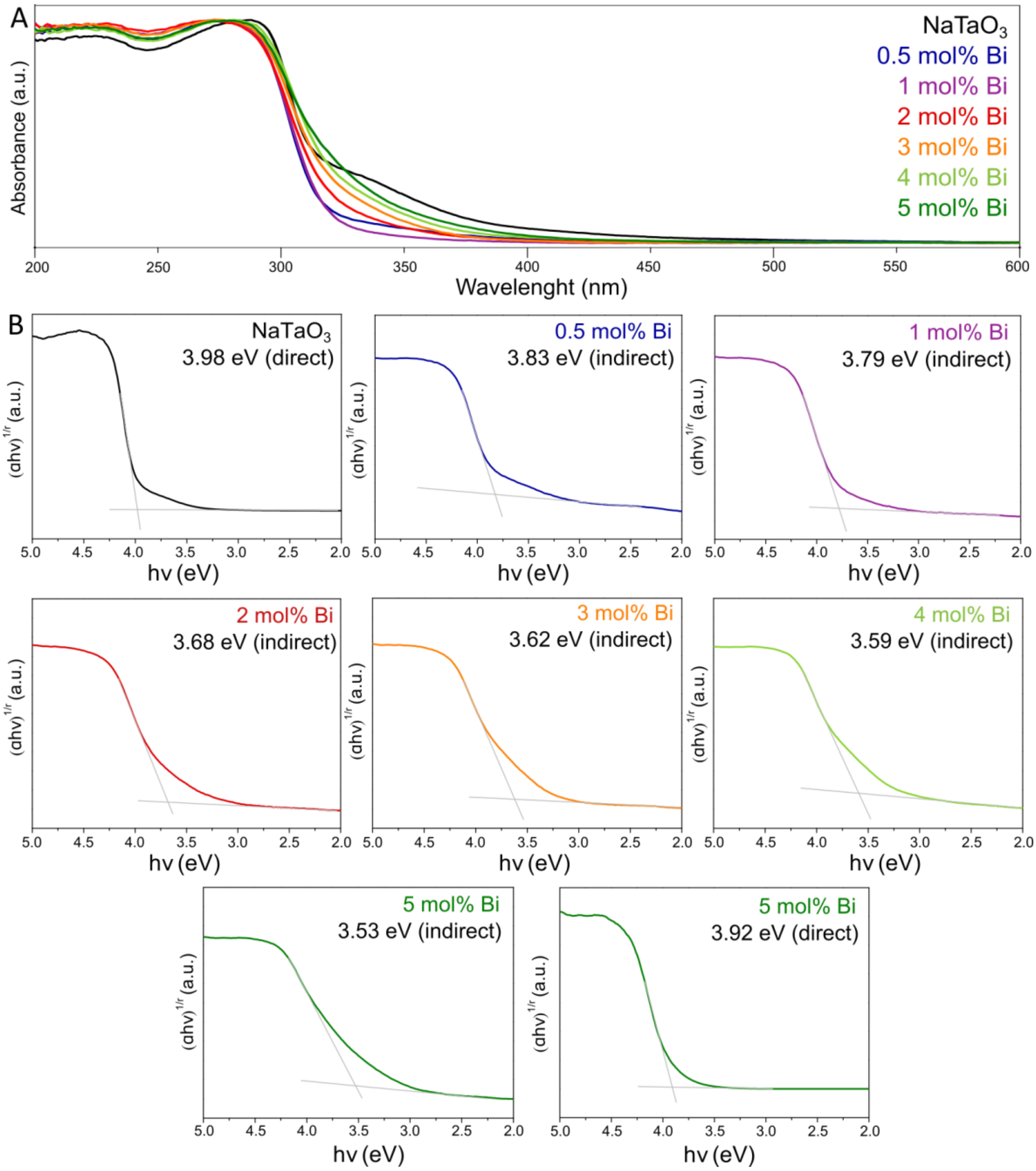

Figure 32 – UV-vis absorption spectra (a) and Tauc plots derived from each spectrum, considering different values for the r coefficient depending on the nature of the optical transition in Bi-doped and pristine $NaTaO_3$ (b)

Source: By the author

Seeking to better understand the contribution of the Bi-doped pseudocubic phase to the electronic structure of the photocatalysts, theoretical modelling based on Density Functional Theory (DFT) have been performed by collaborators Mateus M Ferrer and Julio R. Sambrano. [101] Calculations were carried out using the B3LYP hybrid functional in the CRYSTAL17 package. [102] The models were built from a 2 × 2 × 2 supercell, taking into account the balance between doping magnitude in relation to the experimental value and computational demand for performing the calculations, in order that the Bi-Ta replacement represents a theoretical doping of 12.5%.

In Figures 33a, the band structure of pristine orthorhombic $NaTaO_3$ (JCPDS 73-878) exhibits a direct optical transition of 4.33 eV, which is comparable to the typical calculated and experimental values.[52,84] Furthermore, the density of states plot in Figure 33b confirms that valence band maximum levels consist primarily of O 2p orbitals, while the conduction band minimum is mainly composed of Ta d orbitals.

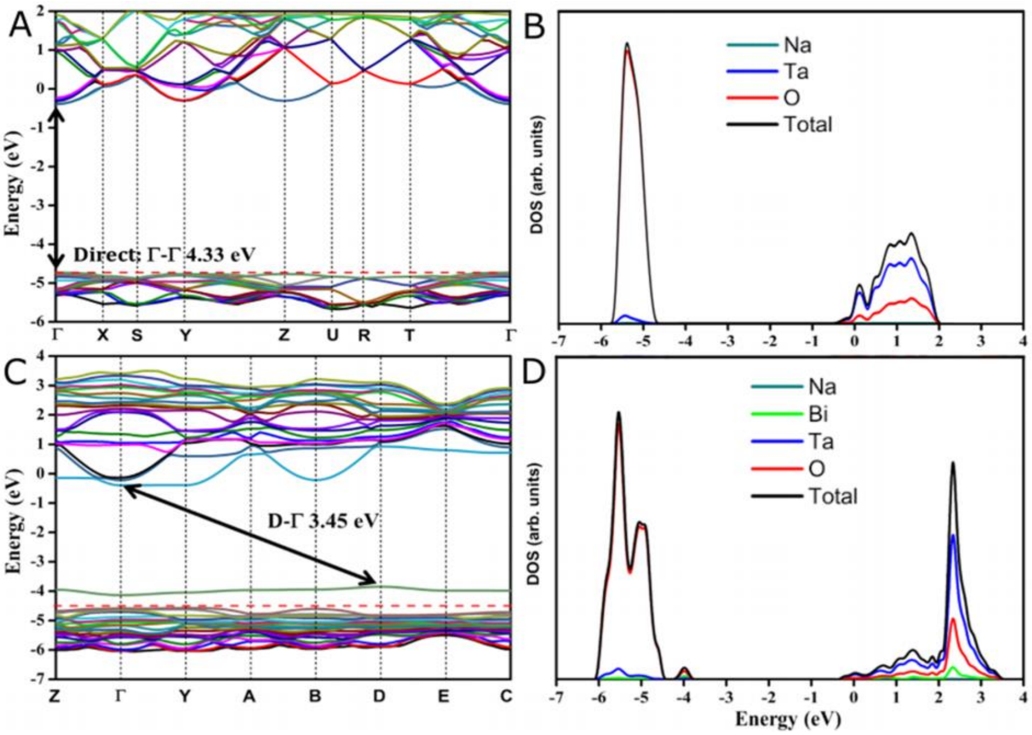

Figure 33 - Electron band structure and density of states calculated for pristine orthorhombic $NaTaO_3$ (a, b) and pseudocubic Bi-Ta doped $NaTaO_3$ with O vacancies. (c, d) The dashed line marks the valence band maximum level of the pure model, in order to highlight the position of the energy level introduced by doping.

Source: By the author

In correspondence to the experimental observations, the doped system was modelled considering the Bi^{3+}-Ta^{5+} substitution in a pseudocubic lattice (JCPDS 74-2479), with the addition O^{2-} vacancies for charge balance. Accordingly, in Figure 33c, the band structure of Bi-doped $NaTaO_3$ is significantly altered with respect to the pure material. The introduction of these defects promote a considerable band gap narrowing of 3.45 eV in virtue of new electronic states near the valence band maximum, which are derived from Bi s and O p orbitals, as shown in Figure 33d. Therefore, this effect can be regarded as a consequence of the periodicity break induced by Bi-Ta substitution, in addition to the polarization between TaO_6 and BiO_5 clusters. Moreover, the introduced midgap state also promotes an indirect (D-Γ) optical transition.

It is important to point out that Na-site doping and Na vacancies may also occur to some extent. However, the influence of these defects on the optical absorption properties of the material is expected to be far less significant than Ta-site and O-site defects, as the localized Na s orbitals do not contribute substantially to the valence and conduction band levels. Furthermore, even though the proposed model for Bi-Ta doping is based upon a higher doping concentration than the real system, the experimental UV-vis absorption data is in reasonable agreement with the calculated band gap values.

In order to evaluate photocatalytic hydrogen evolution under simulated sunlight, Bi-doped $NaTaO_3$ was dispersed in a $H_2O + CH_3OH$ system and irradiated with simulated sunlight spectrum. As expected, Figure 34a shows that $NaTaO_3$ produces only a negligible amount of H_2, in virtue of its wide band gap of 4 eV. However, with the addition of Bi as a dopant, hydrogen evolution is greatly enhanced, as Bi-doped samples exhibit a narrowed band gap. Hydrogen production is already significant even for Bi-doped $NaTaO_3$ with the low dopant concentrations of 0.5, 1 and 2 mol% Bi, with an optimized photocatalytic activity in the sample with 3 mol% Bi, which presents a 0.62 μmol/h H_2 evolution rate. As the Bi proportion is increased to 4 and 5 mol%, hydrogen production is considerably diminished, possibly in virtue of worsened charge separation due to the prominent defects induced by doping, in addition to the presence of surface Bi_2O_3, which may not contribute positively for H_2 evolution.

The remarkable photocatalytic activity of 3 mol% Bi-doped $NaTaO_3$ can be associated to the combination of its narrowed band gap of 3.6 eV with the pseudocubic lattice, as these properties may promote the absorption of photons from simulated sunlight with lower electron-hole recombination rates, as an outcome of the rectified Ta-O-Ta bond angles and the indirect optical transition. Therefore, the proposed mechanism for this enhancement is illustrated in Figure 34b, considering Bi^{3+}-Ta^{5+} atomic substitutions and the formation of oxygen vacancies for charge balance, in correspondence with the experimental and theoretical results presented in this work.

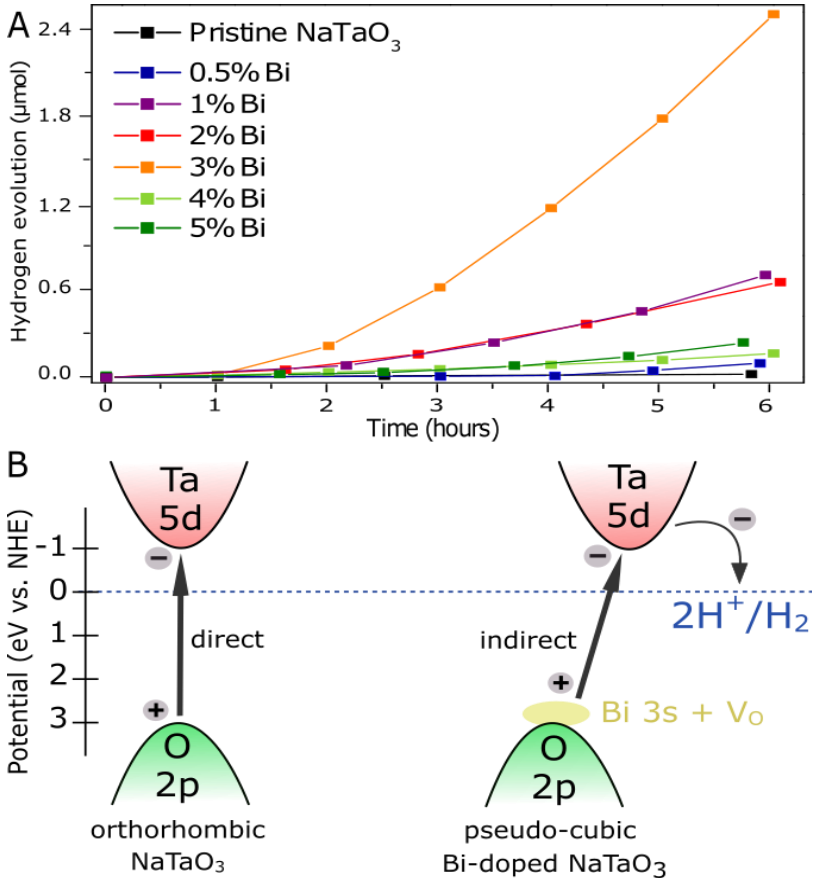

Figure 34 – Photocatalytic hydrogen evolution in H2O + 20 vol% CH3OH for 25mg of Bi-doped $NaTaO_3$ under Xe 300W + AM 1.5G irradiation, at a power of 300 mW/cm2 (a) and schematic band diagram with the proposed charge transfer mechanism for Bi-doped $NaTaO_3$ under AM 1.5G irradiation (b)
Source: By the author

Alternatively, in order to verify the contribution of the molten salt method to the photocatalytic hydrogen evolution, 3 mol% Bi-doped $NaTaO_3$ was produced at the same calcination temperature by a conventional solid state synthesis method, which does not involve the addition of NaCl. As shown in Figure 35, the photocatalytic activity of this sample is expressively lower in comparison to the material obtained by the molten salt method.

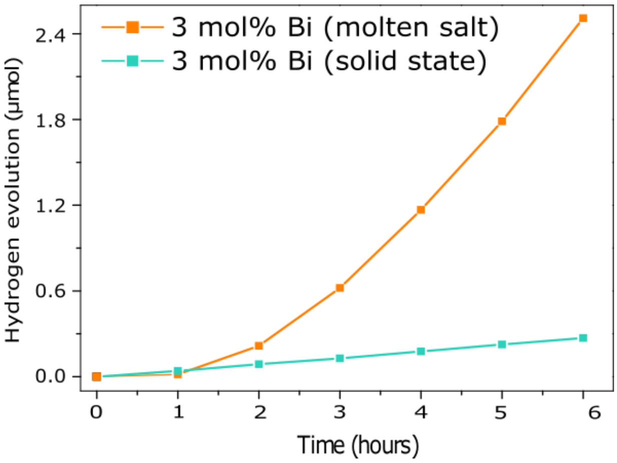

Figure 35 - Photocatalytic hydrogen evolution in H2O + 20 vol% CH3OH for 25mg of 3 mol% Bi-doped $NaTaO_3$ produced by different methods, under Xe 300W + AM 1.5G irradiation, at a power of 300 mW/cm2
Source: By the author

The X-ray diffraction spectrum of the 3 mol% Bi-doped sample produced by the solid state method is shown at Figure 36a, demonstrating that the material exhibits the characteristic pattern of the perovskite oxide, as expected. Comparing these results with the sample obtained by the molten salt synthesis, Figure 36b further indicates the close similarity between the peaks located around 40°, 58° and 68°, which give evidence of the pseudocubic structure. Since the materials exhibit a very similar crystal structure, the superior hydrogen evolution promoted by the molten salt sample cannot be simply ascribed to structural properties. Accordingly, this enhancement is probably a result of the nanocubic morphology, which features exposed facets and a large surface area for the photocatalytic reactions.

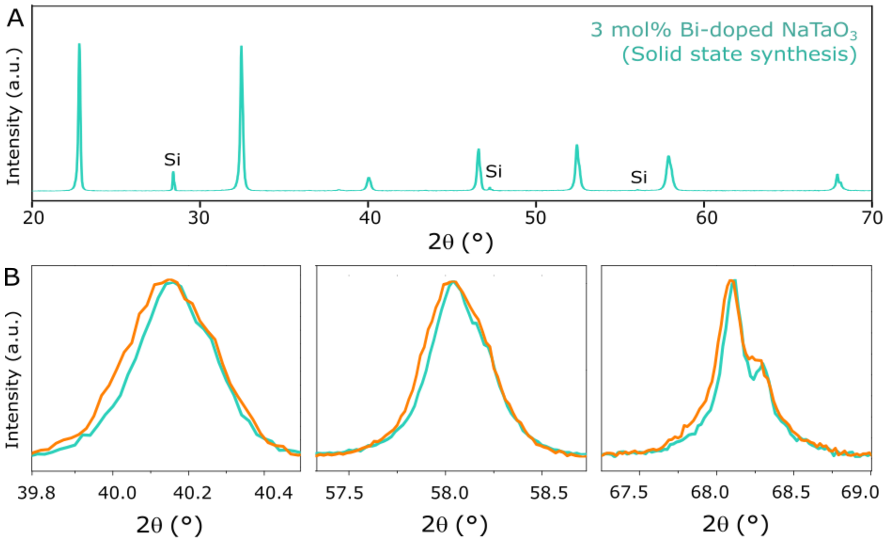

Figure 36 - XRD spectrum of 3 mol% Bi-doped $NaTaO_3$ produced by the solid state method at 1000°C (a) and highlighted regions in the XRD pattern, comparing the material obtained by solid state (blue) and molten salt (orange) showing the pseudocubic phase for both samples. (b)
Source: By the author

3.3 Sputtering deposition of Ni co-catalysts over Bi-doped $NaTaO_3$

As a strategy to provide abundant surface reaction sites for a more efficient hydrogen evolution, Ni co-catalysts were loaded on 3 mol% Bi-doped $NaTaO_3$ samples by magnetron sputtering deposition.[78] Since this method typically produces particles with a size in the range of 10 nm, achieving a precise characterization of the deposited material is a challenging task. However, XPS and TEM methods can elucidate some important aspects of the Ni nanoparticles.

In Figure 37a, the quantification of peak areas indicates that sputtering deposition during 10 min leads to a Ni surface concentration of 16%, with respect to Ta. This indicates that the deposited material occupies a small but significant fraction of the sample surface, as expected for an effective cocatalyst. In the high-resolution spectrum, Ni 2p doublets in Figure 37b reveals the presence of oxidized Ni species on the surface of the sputtered particles. In addition to the typical satellite peaks, the spectrum shows two doublets that can be ascribed to the Ni^{2+} oxidation state. Even though metallic Ni is initially deposited by sputtering deposition, the high surface area of the nanoparticles facilitates surface oxidation after the material is exposed to atmospheric air, thereby leading to the formation of NiO and $Ni(OH)_2$.[103]

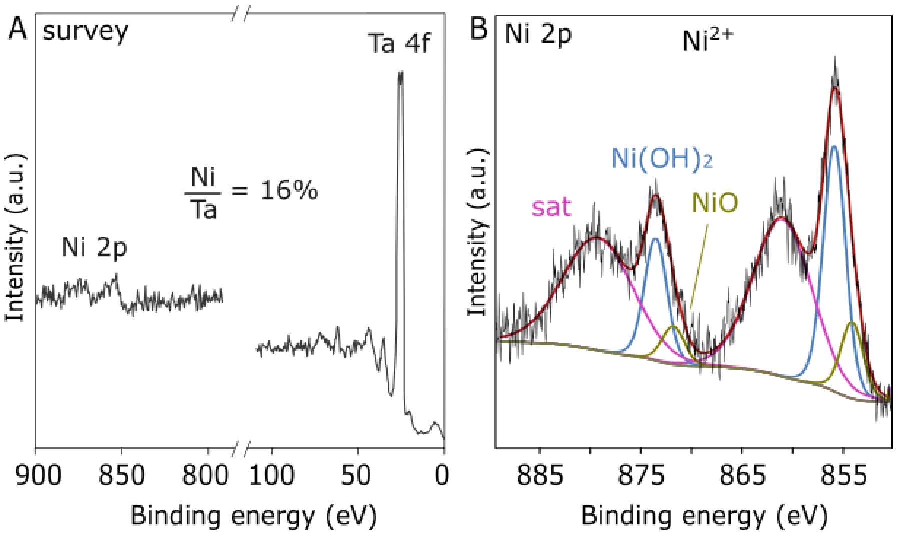

Figure 37 – XPS survey spectrum comparing the surface concentration of Ni and Ta (a) XPS high-resolution spectrum of Ni 2p in 3 mol% Bi-doped $NaTaO_3$ deposited with Ni for 10 min (b)
Source – By the author

In correspondence with the observation of Bi-doped $NaTaO_3$, EDS elemental mapping in Figure 38 shows that Na, Ta and O atoms are evenly dispersed in the material, similarly as observed for the dopant Bi. Moreover, the Ni particles obtained by sputtering deposition are shown to be mostly amorphous, nanosized and well dispersed in the surface of Bi-doped $NaTaO_3$.

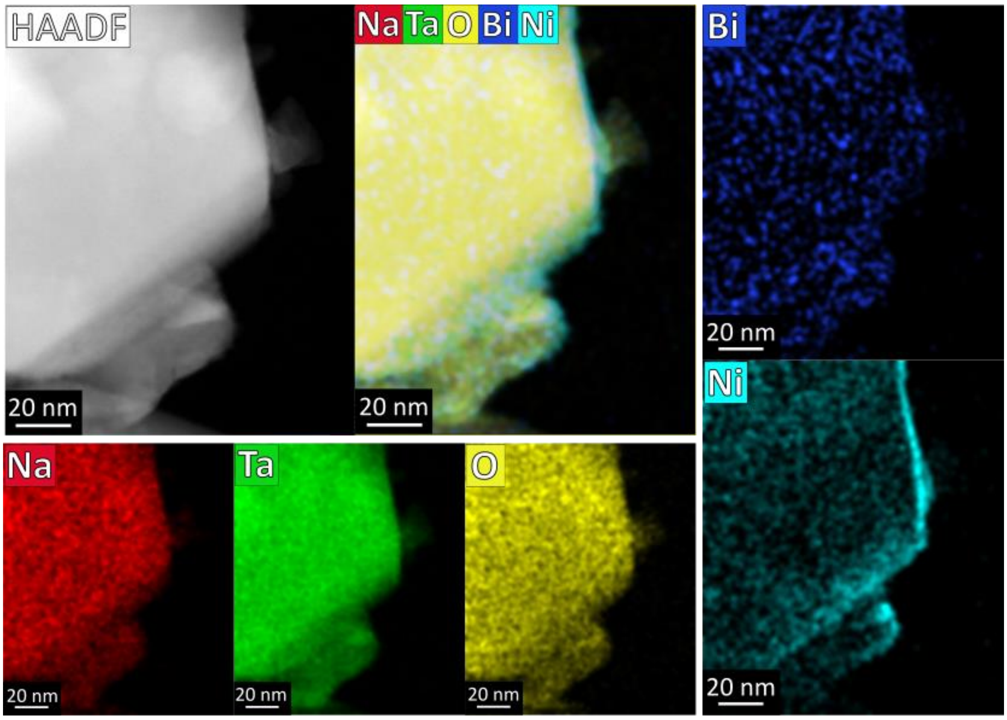

Figure 38 – HAADF image with EDS mapping, showing the elemental composition of 3 mol% Bi-doped $NaTaO_3$ loaded with Ni nanoparticles

Source: By the author

The sputtered nanoparticles are able to substantially improve photocatalytic hydrogen production in 3 mol% Bi-doped $NaTaO_3$, as shown in Figure 39a. Considering the first 7 hours of reaction, the H_2 evolution rate is approximately increased from 0.6 μmol/h to 0.8, 1.7 and 0.9 μmol/h for 5, 10 and 20-minute deposition procedures, respectively. This enhancement indicates that the deposited material acts as a co-catalyst for H_2 evolution, in order that a considerable fraction of photogenerated electrons may be effectively driven from Bi-doped $NaTaO_3$ towards surface Ni particles, where the reduction of protons may take place, [76-77] as illustrated in Figure 39c.

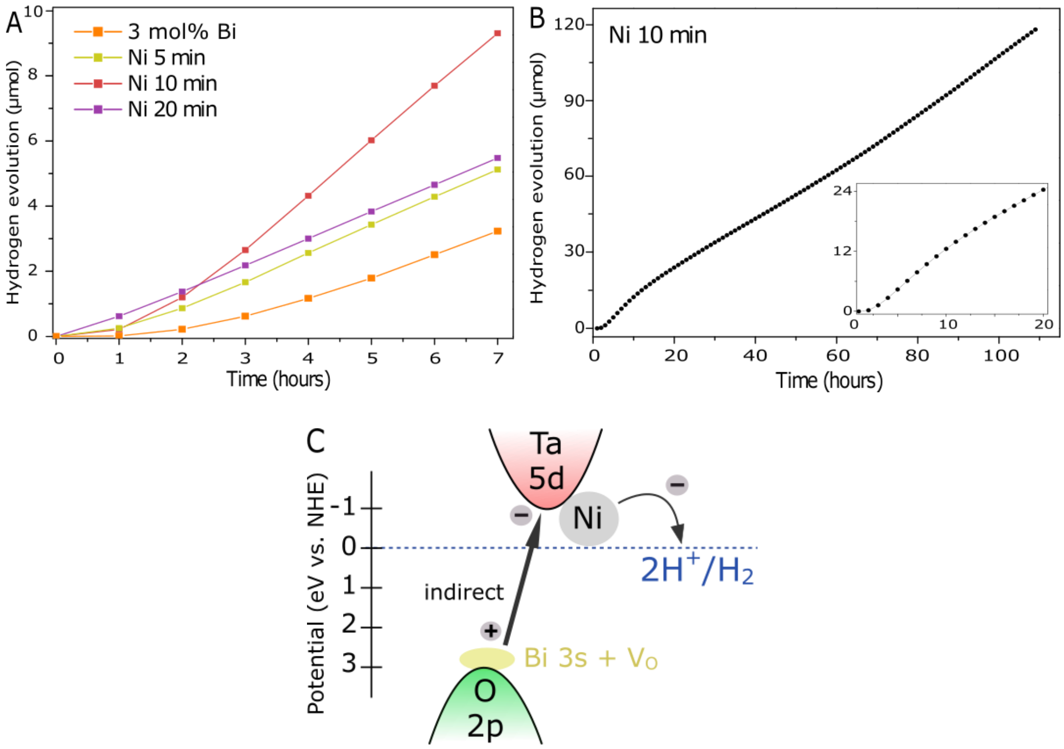

Figure 39 - Photocatalytic hydrogen evolution in H_2O + 20 vol% CH_3OH for Ni-loaded Bi-doped $NaTaO_3$ under Xe 300W + AM 1.5G irradiation, at a 300 mW/cm^2 power for varied sputtering deposition times (a) and during 100h of reaction (b), with the proposed charge transport mechanism (c)
Source: By the author

Figure 39b demonstrates that 3 mol% Bi-doped $NaTaO_3$ with Ni co-catalysts exhibits high stability over 110h of the hydrogen evolution reaction. Although the initial H_2 production rate is in the range of 1.7 µmol/h during the first hours of reaction, this value drops to 1.0 µmol/h after 10 hours and remains considerably constant for the following 100h. This effect can be ascribed to the oxidation of Ni nanoparticles in the aqueous environment, given that NiO_x species are less efficient as a co-catalyst for H_2 evolution, due to their lower conductivity with respect to metallic nickel.

4 CONCLUSIONS

In this work, it has been demonstrated that Bi-doping of $NaTaO_3$ can be an effective strategy for achieving photocatalytic hydrogen production under simulated sunlight. This effect is primarily allowed by Bi^{3+}/Ta^{5+} atomic substitutions, which promote band gap narrowing through the introduction of midgap electron states. Simultaneously, low-concentration doping also leads to a beneficial structural transition for charge carrier separation, as the orthorhombic perovskite becomes pseudocubic. Accordingly, at 3 mol% Bi-doping, the material exhibits a pseudocubic lattice and an indirect band gap of 3.6 eV, in order that these factors may be directly associated with the optimal H_2 evolution of 0.6 μmol/h obtained under AM 1.5G irradiation. Furthermore, magnetron sputtering deposition of Ni nanoparticles is able to considerably enhance the photocatalytic activity, as the material acts as a stable co-catalyst for hydrogen evolution.

In summary, considering the significant challenge of performing solar water splitting, our findings in this study may provide new insights for future developments involving perovskite oxide photocatalysts. Due to their substantial novelty, our results involving Bi-doped $NaTaO_3$ have been recently reported in an article. [101]

In future studies, it will be important to shed light on new strategies to combine Bi-doped $NaTaO_3$ with a wider range of cocatalysts, seeking to achieve overall water splitting from pure water. Whereas Ni has been shown to be effective for hydrogen evolution, the introduction of metal oxide cocatalysts for oxygen evolution may consist in a promising approach towards overall water splitting under natural sunlight.

REFERENCES[*]

1 WRANGHAM, R.; CARMODY, R. Human adaptation to the control of fire. **Evolutionary Anthropology**, v. 19, n. 5, p. 187–199, 2010.

2 MOREHART, C. T.; LENTZ, D. L.; PRUFER, K. M. Wood of the gods: the ritual use of pine (Pinus spp.) by the ancient lowland maya. **Latin American Antiquity**, v. 16, n. 3, p. 255–274, 2005.

3 SMIL, V. World history and energy. *In*: CLEVELAND, C. (ed.). **Encyclopedia of Energy**. New York: Elsevier, 2004. v. 6. p. 549–561.

4 DODSON, J. *et al*. Use of coal in the bronze age in China. **Holocene**, v. 24, n. 5, p. 525–530, 2014.

5 CONNAN, J. Use and trade of bitumen in antiquity and prehistory: molecular archaeology reveals secrets of past civilizations. **Philosophical Transactions of the Royal Society B**: biological Sciences, v. 354, n. 1379, p. 33–50, 1999.

6 RIVERA, J. D. D.; DAVIES, G. M.; JAHN, W. Flammability and the heat of combustion of natural fuels: a review. **Combustion Science and Technology**, v. 184, n. 2, p. 224–242, 2012.

7 LLOYD, W. G.; DAVENPORT, D. A. Applying thermodynamics to fossil fuels: heats of combustion from elemental compositions. **Journal of Chemical Education**, v. 57, n. 1, p. 56–60, 1980.

8 WRIGLEY, E. A. Energy and the english industrial revolution. **Philosophical Transactions of the Royal Society A**: mathematical, physical and engineering sciences, v. 371, n. 1986, p. 1–272, 2013.

9 SMIL, V. **Energy transitions**: global and national perspectives. 2nd ed. Heinemann: Praeger, 2016.

10 SOLOMON, S.; MANNING, M.; MARQUIS M.; QIN, D. (ed.). **Climate Change 2007**: the physical science basis. Contribution of working group I to the fourth assessment report of the intergovernmental panel on climate change. Cambridge: Cambridge University Press, 2007.

11 DIGNON, J. NOx and SOx emissions from fossil fuels: a global distribution. **Atmospheric Environment Part A, General Topics**, v. 26, n. 6, p. 1157–1163, 1992.

12 HOPE, C.; GILDING, P.; ALVAREZ, J. Quantifying the implicit climate subsidy received by leading fossil fuel companies. **Cambridge Judge Business School Working Papers**, n. 2, p. 1–12, 2015.

13 NOROUZI, N.; FANI, M.; ZIARANI, Z. K. The fall of oil age: a scenario planning approach over the last peak oil of human history by 2040. **Journal of Petroleum Science and Engineering**, v. 188, p. 106827, 2020. DOI: 10.1016/j.petrol.2019.106827.

14 BARDI, U. Peak oil, 20 years later: failed prediction or useful insight? **Energy Research and Social Science**, v. 48, p. 257–261, 2019. DOI: 10.1016/j.erss.2018.09.022.

---

[*] According to the ABNT referencing system

15 EIA. **Passenger travel accounts for most of world transportation energy use**. Available from: https://www.eia.gov/todayinenergy/detail.php?id=23832. Accessible at: 2 Oct. 2020.

16 NASA. **Global climate change - vital signs of the planet - carbon dioxide**. Available from: https://climate.nasa.gov/vital-signs/carbon-dioxide. Accessible at: 3 Oct. 2020.

17 SHARMA, S.; GHOSHAL, S. K. Hydrogen the future transportation fuel: from production to applications. **Renewable and Sustainable Energy Reviews**, v. 43, p. 1151–1158, 2015. DOI: 10.1016/j.rser.2014.11.093.

18 EWAN, B. C. R.; ALLEN, R. W. K. A figure of merit assessment of the routes to hydrogen. **International Journal of Hydrogen Energy**, v. 30, n. 8, p. 809–819, 2005.

19 FUJISHIMA, A.; HONDA, K. Electrochemical photolysis of water at a semiconductor electrode. **Nature**, v. 238, n. 5358, p. 37–38, 1972.

20 KUDO, A.; MISEKI, Y. Heterogeneous photocatalyst materials for water splitting. **Chemical Society Reviews**, v. 38, n. 1, p. 253–278, 2009.

21 CHEN, S.; THIND, S.; CHEN, A. Nanostructured materials for water splitting - state of the art and future needs: a mini-review. **Electrochemistry Communications**, v. 63, p. 10–17, 2016. DOI: 10.1016/j.elecom.2015.12.003.

22 HOLGATE, S. A. **Understanding solid state physics**. Boca Raton, FL: Taylor & Francis, 2010.

23 ASHCROFT, N. W.; MERMIN, N. D. **Solid state physics**. New York: Harcourt, 1976.

24 HANAOR, D. A. H. *et al*. Ab initio study of phase stability in doped TiO2. **Computational Mechanics**, v. 50, n. 2, p. 185–194, 2012.

25 WIKIMEDIA COMMONS. **Solid state electronic band structure**. Available from: https://commons.wikimedia.org/wiki/File:Solid_state_electronic_band_structure.svg. Accessible at: 3 Oct. 2020.

26 ZHANG, C. *et al*. Substitutional position and insulator-to-metal transition in Nb-doped SrTiO3. **Materials Chemistry and Physics**, v. 107, n. 2–3, p. 215–219, 2008.

27 HISATOMI, T.; KUBOTA, J.; DOMEN, K. Recent advances in semiconductors for photocatalytic and photoelectrochemical water splitting. **Chemical Society Reviews**, v. 43, n. 22, p. 7520–7535, 2014.

28 CHEN, S.; TAKATA, T.; DOMEN, K. Particulate photocatalysts for overall water splitting. **Nature Reviews Materials**, v. 2, p. 1–17, 2017. DOI: 10.1038/natrevmats.2017.50.

29 NATIONAL RENEWABLE ENERGY LAB. **Reference solar spectral irradiance**: air mass 1.5G. Available from: http://rredc.nrel.gov/solar/spectra/am1.5. Accessible at: 4 Oct. 2020.

30 LU, Q. *et al*. 2D transition-metal-dichalcogenide-nanosheet-based composites for photocatalytic and electrocatalytic hydrogen evolution reactions. **Advanced Materials**, v. 28, n. 10, p. 1917–1933, 2016.

31 KALANUR, S. S. *et al*. Enhancement of photoelectrochemical water splitting response of WO3 by means of Bi doping. **Journal of Catalysis**, v. 357, p. 127–137, 2018. DOI: 10.1016/j.jcat.2017.11.012.

32 MELO, M. A. *et al*. Pseudobrookite Fe2TiO5 nanoparticles loaded with earth-abundant nanosized NiO and Co3O4 cocatalysts for photocatalytic O2 evolution via solar water splitting. **ACS Applied Nano Materials**, v. 3, n. 9, p. 9303–9317, 2020.

33 LI, R.; LI, C. Photocatalytic water splitting on semiconductor-based photocatalysts. **Advances in Catalysis**, v. 60, p. 1-57, 2017. DOI: 10.1016/bs.acat.2017.09.001.

34 GRABOWSKA, E. Selected perovskite oxides: characterization, preparation and photocatalytic properties - a review. **Applied Catalysis B**: environmental, v. 186, p. 97–126, 2016. DOI: 10.1016/j.apcatb.2015.12.035

35 ISHIHARA, T. **Perovskite oxide for solid oxide fuel cells.** New York: Springer, 2009. (Fuel cells and hydrogen energy)

36 TRAVIS, W. *et al.* On the application of the tolerance factor to inorganic and hybrid halide perovskites: a revised system. **Chemical Science**, v. 7, n. 7, p. 4548–4556, 2016.

37 YANG, C.; GRIMAUD, A. Factors controlling the redox activity of oxygen in perovskites: from theory to application for catalytic reactions. **Catalysts**, v. 7, n. 149, p. 1–27, 2017.

38 DOLGOS, M. *et al*. Chemical control of octahedral tilting and off-axis A cation displacement allows ferroelectric switching in a bismuth-based perovskite. **Chemical Science**, v. 3, n. 5, p. 1426–1435, 2012.

39 LU, W. *et al*. The role of octahedral tilting in the structural phase transition and magnetic anisotropy in SrRuO3 thin film. **Journal of Applied Physics**, v. 113, n. 6, p. 0–7, 2013.

40 KATO, H.; KUDO, A. Highly efficient decomposition of pure water into H2 and O2 over NaTaO3 photocatalysts. **Catalysis Letters**, v. 58, n. 2, p. 153–155, 1999.

41 KATO, H.; KUDO, A. Water splitting into H2 and O2 on alkali tantalate photocatalysts ATaO3 (A = Li, Na, and K). **Journal of Physical Chemistry B**, v. 105, n. 19, p. 4285–4292, 2001.

42 LEE, S. *et al*. Growth of well-developed sodium tantalate crystals from a sodium chloride flux. **CrystEngComm**, v. 12, n. 10, p. 2871–2877, 2010.

43 SHI, J. *et al*. Microwave-assisted hydrothermal synthesis of perovskite NaTaO3 nanocrystals and their photocatalytic properties. **Journal of Materials Chemistry**, v. 22, n. 36, p. 18808–18813, 2012.

44 WU, X. *et al*. A carbon modified NaTaO3 mesocrystal nanoparticle with excellent efficiency of visible light induced photocatalysis. **Journal of Materials Chemistry A**, v. 2, n. 48, p. 20832–20840, 2014.

45 HUERTA-FLORES, A. M. *et al*. Laser assisted chemical vapor deposition of nanostructured NaTaO3 and SrTiO3 thin films for efficient photocatalytic hydrogen evolution. **Fuel**, v. 197, p. 174–185, 2017. DOI: 10.1016/j.fuel.2017.02.016.

46 FRESNO, F. *et al.* CO2 reduction over NaNbO3 and NaTaO3 perovskite photocatalysts. **Photochemical and Photobiological Sciences**, v. 16, n. 1, p. 17–23, 2017.

47 ONISHI, H. Sodium tantalate photocatalysts doped with metal cations : why are they active for water splitting? **ChemSusChem**, v. 12, p. 1825–1834, 2019. DOI: 10.1002/cssc.201802935.

48 MODAK, B.; SRINIVASU, K.; GHOSH, S. K. Photocatalytic activity of NaTaO3 doped with N, Mo, and (N,Mo): a hybrid density functional study. **Journal of Physical Chemistry C**, v. 118, n. 20, p. 10711–10719, 2014.

49 KNIGHT, K. S.; KENNEDY, B. J. Phase coexistence in NaTaO3 at room temperature: a high resolution neutron powder diffraction study. **Solid State Sciences**, v. 43, p. 15–21, 2015. DOI: 10.1016/j.solidstatesciences.2015.03.016.

50 ARULNESAN, S. W. *et al*. Phase separation in NaTaO3: impact of temperature and doping. **Solid State Sciences**, v. 52, p. 149–153, 2016. DOI: 10.1016/j.solidstatesciences.2016.01.001.

51 HU, C.; TENG, H. Influence of structural features on the photocatalytic activity of NaTaO 3 powders from different synthesis methods. **Applied Catalysis A**: general, v. 331, p. 44–50, 2007. DOI: 10.1016/j.apcata.2007.07.024.

52 LIN, W. *et al*. NaTaO3 photocatalysts of different crystalline structures for water splitting into H2 and O2. **Applied Physics Letters**, v. 89, n. 21, p. 211904, 2006.

53 HU, C. C.; LEE, Y. L.; TENG, H. Efficient water splitting over Na1-xKxTaO3 photocatalysts with cubic perovskite structure. **Journal of Materials Chemistry**, v. 21, n. 11, p. 3824–3830, 2011.

54 HU, C.-C.; TSAI, C.-C.; TENG, H. Structure characterization and tuning of perovskite-like NaTaO3 for applications in photoluminescence and photocatalysis. **Journal of the American Ceramic Society**, v. 92, n. 2, p. 460–466, 2009.

55 KATO, H.; ASAKURA, K.; KUDO, A. Highly efficient water splitting into H2 and O2 over lanthanum-doped NaTaO3 photocatalysts with high crystallinity and surface nanostructure. **Journal of the American Chemical Society**, v. 125, n. 10, p. 3082–3089, 2003.

56 LIU, X.; SOHLBERG, K. Role of effective carrier mass in the photocatalytic efficiency of La-doped. **Computational Materials Science**, v. 123, p. 1–7, 2016. DOI: 10.1016/j.commatsci.2016.06.013.

57 MIZUTANI, S. *et al*. Charge carrier dynamics in Sr-doped NaTaO3 photocatalysts revealed by deep ultraviolet single-particle microspectroscopy. **Journal of Physical Chemistry C**, v. 123, n. 20, p. 12592–12598, 2019.

58 IWASE, A. *et al*. Formation of surface nano-step structures and improvement of photocatalytic activities of NaTaO 3 by doping of alkaline earth metal ions. **Chemistry Letters** v. 33, n. 10, p. 1260–1261, 2004.

59 YANG, M. *et al*. Improved hydrogen evolution activities under visible light irradiation over NaTaO 3 codoped with lanthanum and chromium. **Materials Chemistry and Physics**, v. 121, n. 3, p. 506–510, 2010.

60 KANHERE, P. *et al*. Electronic structure, optical properties, and photocatalytic activities of LaFeO3–NaTaO3 solid solution. **Journal of Physical Chemistry C**, v. 116, n. 43, p. 22767–22773, 2012.

61 JOO, P. H.; BEHTASH, M.; YANG, K. Energetic stability, oxidation states and electronic structure of Bi-doped NaTaO3: a first-principles hybrid functional study. **Physical Chemistry Chemical Physics**, v. 18, n. 2, p. 857–865, 2016.

62 LI, Z. *et al*. Photocatalytic hydrogen production from aqueous methanol solutions under visible light over Na(Bi x Ta 1-x) O3. **International Journal of Hydrogen Energy**, v. 34, n. 1, p. 147–152, 2009.

63 KANG, H. W.; LIM, S. N.; PARK, S. BIN. Photocatalytic H2 evolution under visible light from aqueous methanol solution on NaBixTa1−xO3 prepared by spray pyrolysis. **International Journal of Hydrogen Energy**, v. 37, n. 5, p. 4026–4035, 2012.

64 KANHERE, P.; ZHENG, J.; CHEN, Z. Visible light driven photocatalytic hydrogen evolution and photophysical properties of Bi3+ doped NaTaO3. **International Journal of Hydrogen Energy**, v. 37, n. 6, p. 4889–4896, 2012.

65 LI, X.; ZANG, J. Facile hydrothermal synthesis of sodium tantalate (NaTaO3) nanocubes and high photocatalytic properties. **Journal of Physical Chemistry C**, v. 113, n. 45, p. 19411–19418, 2009.

66 KIMURA, T. Molten salt synthesis of ceramic powders. *In:* SIKALIDIS, C. (ed.). **Advances in ceramics**: synthesis and characterization, processing and specific applications. Rijeka, Croatia: InTech, 2011. p. 75–76.

67 FU, J. *et al*. Improving dielectric properties of PVDF composites by employing surface modified strong polarized BaTiO3 particles derived by molten salt method. **ACS Applied Materials and Interfaces**, v. 7, n. 44, p. 24480–24491, 2015.

68 LEE, S. *et al*. Growth of well-developed sodium tantalate crystals from a sodium chloride flux. **CrystEngComm**, v. 12, n. 10, p. 2871–2877, 2010.

69 AFROZ, K. *et al*. A heterojunction strategy to improve the visible light sensitive water splitting performance of photocatalytic materials. **Journal of Materials Chemistry A**, v. 6, n. 44, p. 21696–21718, 2018.

70 RANA, F. **Semiconductor optoelectronics, chapter 2**: semiconductor heterostructures. Available from: courses.cit.cornell.edu/ece533/Lectures/handout2.pdf. Accessible at: 6 Oct. 2020.

71 ZHANG, Z.; YATES, J. T. Band bending in semiconductors: chemical and physical consequences at surfaces and interfaces. **Chemical Reviews**, v. 112, n. 10, p. 5520–5551, 2012.

72 POLETI, D. *et al*. Mechanochemical synthesis of γ-Bi 2 O 3. **Solid State Sciences**, v. 6, n. 3, p. 239–245, 2004.

73 YANG, J. *et al*. Roles of cocatalysts in photocatalysis and photoelectrocatalysis. **Accounts of Chemical Research.**, v. 46, n. 8, p. 1900–1909, 2013.

74 CAO, S. *et al*. Metal phosphides as co-catalysts for photocatalytic and photoelectrocatalytic water splitting. **ChemSusChem**, v. 10, n. 22, p. 4306–4323, 2017.

75 BAI, S. *et al*. Surface and interface engineering in photocatalysis. **ChemNanoMat**, v. 1, n. 4, p. 223–239, 2015.

76 ZHANG, Q. *et al*. Effect of redox cocatalysts location on photocatalytic overall water splitting over cubic NaTaO3 semiconductor crystals exposed with equivalent facets. **ACS Catalysis**, v. 6, n. 4, p. 2182–2191, 2016.

77 HU, C. C.; TENG, H. Structural features of p-type semiconducting NiO as a co-catalyst for photocatalytic water splitting. **Journal of Catalysis**, v. 272, n. 1, p. 1–8, 2010.

78 GONÇALVES, R. V. *et al*. Photochemical hydrogen production of Ta2O5 nanotubes decorated with NiO nanoparticles by modified sputtering deposition. **Journal of Physical Chemistry C**, v. 121, n. 11, p. 5855–5863, 2017.

79 SIM, Y. *et al*. Efficient photoelectrochemical water splitting reaction using electrodeposited Co3Se4 catalyst. **Applied Sciences (Switzerland)**, v. 9, n. 1, p. 16, 2018.

80 KELLY, P. J.; ARNELL, R. D. Magnetron sputtering: a review of recent developments and applications. **Vacuum**, v. 56, n. 3, p. 159–172, 2000.

81 WENDER, H. *et al*. Sputtering onto liquids: from thin films to nanoparticles. **Journal of Physical Chemistry C**, v. 115, n. 33, p. 16362–16367, 2011.

82 GONÇALVES, R. V. *et al*. Easy access to metallic copper nanoparticles with high activity and stability for CO oxidation. **ACS Applied Materials and Interfaces**, v. 7, n. 15, p. 7987–7994, 2015.

83 XIAO, G. **Magnetron sputtering technology summary**. Available from: https://www.brown.edu/research/labs/xiao/magnetic-sputtering-technology-summary. Accessible at: 19 Feb. 2021.

84 KATO, H.; KUDO, A. Highly efficient decomposition of pure water into H2 and O2 over NaTaO3 photocatalysts. **Catalysis Letters**, v. 58, n. 2–3, p. 153–155, 1999.

85 YE, L. *et al*. The thermal physical properties and stability of the eutectic composition in a Na2CO3-NaCl binary system. **Thermochimica Acta**, v. 596, p. 14–20, 2014. DOI: 10.1016/j.tca.2014.07.002.

86 ORTIZ-QUIÑONEZ, J. L. *et al*. Transformation of bismuth and β-Bi2O3 nanoparticles into (BiO)2CO3 and (BiO)4(OH)2CO3 by capturing CO2: the role of halloysite nanotubes and “sunlight” on the crystal shape and size. **Crystal Growth & Design**, v. 18, n. 8, p. 4334–4346, 2018.

87 JIANG, W.; JIAO, X.; CHEN, D. Photocatalytic water splitting of surfactant-free fabricated high surface area NaTaO3 nanocrystals. **International Journal of Hydrogen Energy**, v. 38, n. 29, p. 12739–12746, 2013.

88 ISMAILZADE, I. G. An X-Ray diffraction study of phase transitions in sodium tantalate. **Kristallografiya**, v. 718, n. 7, 1962.

89 OTONICAR, M. *et al*. Analysis of the phase transition and the domain structure in K0.5Bi0.5TiO3 perovskite ceramics by in situ XRD and TEM. **Journal of the American Ceramic Society** v. 93, n. 12, p. 4168–4173, 2010.

90 BHALLA, A. S. *et al*. Raman spectroscopy of Mg-Ta order-disorder in BaMg1/3Ta2/3O3. **Journal of Physics and Chemistry of Solids**, v. 59, n. 2, p. 181–195, 1998.

91 AN, L.; ONISHI, H. Electron–hole recombination controlled by metal doping sites in NaTaO3 photocatalysts. **ACS Catalysis**, v. 5, n. 6, p. 3196–3206, 2015.

92 SUDRAJAT, H. *et a*l. Stability of La dopants in NaTaO3 photocatalysts. **Journal of Alloys and Compounds**, v. 775, p. 1277–1285, 2019. DOI: 10.1016/j.jallcom.2018.10.237.

93 GONÇALVES, R. V. *et al*. Insights into the active surface species formed on Ta2O5 nanotubes in the catalytic oxidation of CO. **Physical Chemistry Chemical Physics**, v. 16, n. 12, p. 5755-5762 2014.

94 YANG, B. S. *et al*. Improvement of the photo-bias stability of the Zn–Sn–O field effect transistors by an ozone treatment. **Journal of Materials Chemistry**, v. 22, p. 10994–10998, 2012. DOI: 10.1039/c2jm30242j.

95 ZHAO, Z. *et al*. Electronic structure basis for enhanced overall water splitting photocatalysis with aluminum doped SrTiO3 in natural sunlight. **Energy & Environmental Science**, v. 12, n. 4, p. 1385–1395, 2019.

96 BLUHM, H. Photoelectron spectroscopy of surfaces under humid conditions. **Journal of Electron Spectroscopy and Related Phenomena**, v. 177, n. 2–3, p. 71–84, 2010.

97 KANHERE, P. D.; ZHENG, J.; CHEN, Z. Site specific optical and photocatalytic properties of Bi-doped NaTaO3. **Journal of Physical Chemistry C**, v. 115, n. 23, p. 11846–11853, 2011.

98 DHARMADHIKARI, V. S. *et al*. Characterisation of thin films of bismuth oxide by X-ray photoelectron spectroscopy. **Journal of Electron Spectroscopy and Related Phenomena**, v. 25, n. 2, p. 181-189, 1982.

99 LIU, X.; SOHLBERG, K. The influence of oxygen vacancies and La doping on the surface structure. **Computational Materials Science**, v. 103, p. 1–7, 2015. DOI: 10.1016/j.commatsci.2015.03.004.

100 DING, Q. *et al*. Unravelling the water oxidation mechanism on NaTaO3–based photocatalyst. **Journal of Materials Chemistry A**, v. 8, n. 14, p. 6812–6821, 2020.

101 ALVES, G. A. S. *et al*. Band gap narrowing of Bi-doped NaTaO3 for photocatalytic hydrogen evolution under simulated sunlight : a pseudocubic phase induced by doping. **ACS Applied Energy Materials**, v. 4, n. 1, p. 671-679, 2020.

102 DOVESI, R. *et al*. Quantum-mechanical condensed matter simulations with CRYSTAL. **WIREs Computational Molecular Science**, v. 8, n. 4, p. e1360, 2018.

103 SALVATI, L. *et al*. Surface spectroscopic study of tungsten-alumina catalysts using x-ray photoelectron, ion scattering, and Raman spectroscopies. **Journal of Physical Chemistry**, v. 85, n. 24, p. 3700–3707, 1981.